J. Fluid Mech. (2024), *vol*. 978, A25, doi:10.1017/jfm.2023.1034

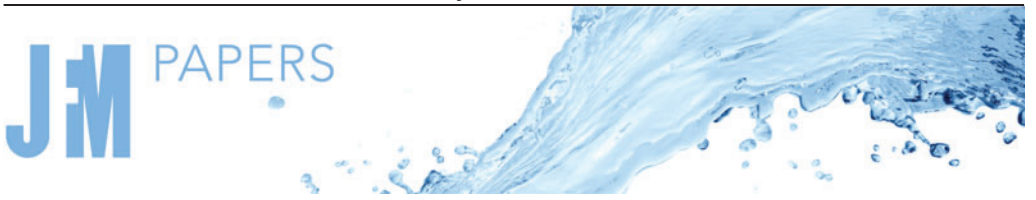

Total and static temperature statistics in compressible turbulent plane channel flow

G.A. Gerolymos[1] **and I. Vallet**[1],†

[1]Faculty of Engineering, Sorbonne Université, 4 place Jussieu, 75005 Paris, France

(Received 14 April 2023; revised 27 October 2023; accepted 28 November 2023)

The paper studies the statistics of total and static temperature (total h_t and static h enthalpy) in compressible turbulent plane channel flow using direct numerical simulations (DNS) data covering the range of centreline Mach numbers $0.3 \lessapprox \bar{M}_{CL_x} \lessapprox 2.5$ and Huang–Coleman–Bradshaw friction Reynolds numbers $100 \lessapprox Re_{\tau^\star} \lessapprox 1000$. For this class of very-cold-wall flows, the DNS data for correlation coefficients and joint probability density functions (p.d.f.s) show that h_t' is invariably very strongly correlated with the streamwise velocity fluctuation u', in contrast to static temperature (static enthalpy h') whose correlation with u' weakens rapidly with increasing wall distance. We study various correlations and joint p.d.f.s of h_t' and h' in relation to the fluctuating velocity field, including the turbulent Prandtl number Pr_T, and discuss the predictions of Reynolds analogy. The scaling of the mean enthalpy and the fluctuating enthalpy variance and fluxes with respect to inner and outer velocity scales is investigated. The complex behaviour and scaling of different terms in the transport equations for the enthalpy variance and fluxes are discussed.

Key words: turbulent boundary layers, compressible turbulence, turbulent convection

1. Introduction

Numerous direct numerical simulations (DNS) studies of compressible wall turbulence, in both channels (Coleman, Kim & Moser 1995; Foysi, Sarkar & Friedrich 2004; Modesti & Pirozzoli 2016; Yao & Hussain 2020) and boundary layers (Duan, Beekman & Martín 2011; Pirozzoli & Bernardini 2013; Zhang, Duan & Choudhari 2018) have provided data for turbulent correlations that are difficult to measure with accuracy near the wall (Smits & Dussauge 2006), and in the case of correlations between higher-order

† Email address for correspondence: isabelle.vallet@sorbonne-universite.fr

derivatives (Gerolymos & Vallet 2014; Suman & Girimaji 2013) are impossible to obtain experimentally. It is somehow surprising that relatively little has been reported on total temperature T_t' (total enthalpy h_t') correlations with the fluctuating velocity field u_i'. The aim of this paper is the systematic study of h_t' statistics in compressible turbulent plane channel (TPC) flow using DNS data.

Independently of the particular bivariate thermodynamics model used for the equation of state, total and static enthalpy are related by

$$h_t := h + \tfrac{1}{2}u_iu_i \implies \begin{cases} \bar{h}_t = \bar{h} + \tfrac{1}{2}\bar{u}_i\bar{u}_i + \tfrac{1}{2}\overline{u_i'u_i'}, \\ h_t' = h' + \bar{u}_iu_i' + \tfrac{1}{2}\left(u_i'u_i' - \overline{u_i'u_i'}\right), \end{cases} \tag{1.1a}$$

readily implying relations for variances and fluxes

$$\overline{h_t'u_i'} = \overline{h'u_i'} + \bar{u}_j\overline{u_j'u_i'} + \overbrace{\tfrac{1}{2}\overline{u_j'u_j'u_i'}}^{3oMs}, \tag{1.1b}$$

$$\overline{h'^2} = \overline{h_t'^2} + \bar{u}_i\bar{u}_j\overline{u_i'u_j'} - 2\overline{h_t'u_i'}\bar{u}_i - \underbrace{\left(\overline{h_t'u_i'u_i'} - \bar{u}_i\overline{u_i'u_j'u_j'}\right)}_{3oMs} + \underbrace{\tfrac{1}{4}\left(\overline{u_i'u_i'u_j'u_j'} - \overline{u_i'u_i'}\;\overline{u_j'u_j'}\right)}_{4oMs}, \tag{1.1c}$$

$$= \overline{h_t'^2} - \bar{u}_i\bar{u}_j\overline{u_i'u_j'} - 2\overline{h'u_i'}\bar{u}_i - \underbrace{\left(\overline{h'u_i'u_i'} + \bar{u}_i\overline{u_i'u_j'u_j'}\right)}_{3oMs} - \underbrace{\tfrac{1}{4}\left(\overline{u_i'u_i'u_j'u_j'} - \overline{u_i'u_i'}\;\overline{u_j'u_j'}\right)}_{4oMs}, \tag{1.1d}$$

where h is the static enthalpy, and $u_i \in \{u, v, w\}$ are the velocity components in a Cartesian reference frame $x_i \in \{x, y, z\}$. The usual notations $(\cdot) = \overline{(\cdot)} + (\cdot)' = \widetilde{(\cdot)} + (\cdot)''$ are adopted for Reynolds or Favre averages and fluctuations, and Einstein's summation convention of repeated indices is applied. The presence of the fluctuation of turbulence kinetic energy $\frac{1}{2}(u_i'u_i')' := \frac{1}{2}u_i'u_i' - \frac{1}{2}\overline{u_i'u_i'}$ in the expression for h_t' in (1.1*a*) introduces higher-order moments (HoMs): 3-order moments (3oMs) for the fluxes (1.1*b*) and also 4-order moments (4oMs) for the variances (1.1*c*). The implication of (1.1) is that total h_t' statistics cannot be reconstructed with DNS accuracy from static h' statistics unless all HoMs are also acquired. It is more practical to sample h_t' statistics directly.

In the classic paper on the strong Reynolds analogy (SRA), Morkovin (1962) identified the assumption of negligible root mean square (r.m.s.) $h_{t_{rms}}'$ as the major structural default of the approximation (Gaviglio 1987), in disagreement with measurements (Kistler 1959). Available data (Guarini *et al.* 2000; Shahab *et al.* 2011) show that for an adiabatic wall ($\bar{T}_w \approxeq T_r$, where T_r is the adiabatic wall recovery temperature), $h_{t_{rms}}'/h_{rms}' = O(1)$ in a large part of the layer. As the wall temperature cools down from the adiabatic wall temperature T_r (it is more precise and Mach-independent to say as the non-dimensional wall flux gradient $[d_{\bar{u}}\bar{h}]_w/\bar{u}_\delta$, where $\bar{u}_\delta$ is the mean velocity at the wall layer edge, increases) the ratio $h_{t_{rms}}'/h_{rms}'$ increases relative to the adiabatic level (Debiève *et al.* 1997, figure 11, p. 56). Turbulent boundary layer (TBL) DNS data (Shahab *et al.* 2011, figure 15, p. 387) for adiabatic ($\bar{T}_w = T_r$) and isothermal ($\bar{T}_w = \bar{T}_\delta = 0.67T_r$) walls shows that there is a very important decrease of h_{rms}' with wall cooling, rather than a strong increase of $h_{t_{rms}}'$. The wall is even cooler for compressible TPC flow, the ratio $T_r/\bar{T}_w$ increasing very strongly with centreline Mach number $\bar{M}_{CL_x}$ (Gerolymos & Vallet 2023, figure 6, p. A19-15), inducing a slight increase of the ratio $h_{t_{rms}}'/h_{rms}'$ (Huang, Coleman & Bradshaw 1995).

In contrast to this relatively small volume of data for h_t' statistics, there is a very large volume of data for the turbulent Prandtl number Pr_T, both experimental (Meier & Rotta 1971; Bagheri, Strataridakis & White 1992; Wardana, Ueda & Mizomoto 1995) and DNS (Coleman *et al.* 1995; Guarini *et al.* 2000; Bernardini & Pirozzoli 2011; Duan *et al.* 2011; Shahab *et al.* 2011; Zhang, Duan & Choudhari 2017; Huang, Duan & Choudhari 2022). These data, covering a wide range of Mach numbers and wall temperature conditions (from very cold to very hot walls) in TBLs and TPCs, indicate that Pr_T diminishes from a value $\sim$1 in the buffer layer to a value $\sim$0.7 in the wake region, showing little sensitivity to the flow conditions. They also show that the wall-normal flux ($\overline{h'v'}$ or $\overline{\rho h''v''}$) is systematically opposed to the temperature gradient $d_y\bar{T}$, whereas the streamwise flux ($\overline{h'u'}$ or $\overline{\rho h''u''}$) is systematically of the same sign as the temperature gradient $d_y\bar{T}$ (Shahab *et al.* 2011, figure 17, p. 388). The data also agree that the absolute value of the streamwise flux correlation coefficient $|c_{h'u'}|$ drops from values near $\sim$0.9 close to the wall to lower values $\lessapprox$0.5 at δ (Guarini *et al.* 2000; Bernardini & Pirozzoli 2011; Huang *et al.* 2022).

These data contradict the SRA, which postulates (Morkovin 1962; Gaviglio 1987; Huang *et al.* 1995) an instantaneous relation $h' \propto u' \Rightarrow |c_{h'u'}| = 1$, independently of the particular proportionality function. Regarding this proportionality function, the most successful choice is due to Huang *et al.* (1995), with the $\mathrm{sgn}(d_{\bar{u}}\bar{h})$ fix of Guarini *et al.* (2000) allowing the accommodation of both cold and hot walls. Gaviglio (1987, (27), p. 915) remarks that truncating to 2-order moments (2oMs), the relations (1.1) imply in parallel flow that $\overline{h_t'^2} \approxeq \overline{h'^2} + \bar{u}^2\overline{u'^2} + 2\bar{u}\,u'_{rms}\,c_{h'u'}$, and show how the value of the correlation coefficient $c_{h'u'}$ (which, as discussed above, admits large variations) impacts the ratio $h'_{t_{rms}}/h'_{rms}$ (Gaviglio 1987, figure 3, p. 916). This relation also implies that when $|c_{h'u'}| \approxeq 1$, whether $h'_{t_{rms}}/h'_{rms} \lesseqgtr 1$ is decided by $\mathrm{sgn}(c_{h'u'})$. However, the departure of $|c_{h'u'}|$ from unity observed in the data can be incorporated only in a correlation-based Reynolds analogy that does not postulate an instantaneous relation between h' and u', but uses relations and approximations for correlations and correlation coefficients instead. Decomposing the instantaneous h' into a correlated (with u') and an uncorrelated part (Zhang *et al.* 2014) does not solve the problem as it requires further assumptions on the uncorrelated part.

To obtain less cold wall conditions while maintaining the computationally advantageous streamwise invariance of the flow, some authors include an artificial heat-sink source term in the energy equation (Coleman *et al.* 1995; Yu, Xu & Pirozzoli 2020; Modesti *et al.* 2022) or apply different upper/lower wall temperatures (Morinishi, Tamano & Nakabayashi 2004; Lusher & Coleman 2022). In the present work, we concentrate on canonical TPC flows (Coleman *et al.* 1995) between symmetric isothermal walls (Song *et al.* 2022).

The DNS database (Gerolymos & Vallet 2023) used to acquire h' statistics and h_t' statistics in compressible TPC flow is described in § 2. In § 3, we discuss the effect of frictional heating on the mean flow and compare with other DNS data available in the literature. In § 4, we study the $(Re_{\tau^\star}, \bar{M}_{CL_x})$ dependence of the profiles of variances (§ 4.3), correlation coefficients (§ 4.4) and joint probability density functions (p.d.f.s) with the streamwise velocity (§ 4.5). The data can be analysed (§ 4.3) in terms of the correlation coefficients for h_t' and h' transport (§ 4.1) and of the turbulent Prandtl number (§ 4.2). In § 5.1, we investigate the accuracy of the SRA for the class of canonical TPC flows studied, and discuss its inherent limitations (§ 5.2). For the canonical TPC flows studied, the very strong (h_t', u') correlation revealed by the DNS data (§ 4.4) can be exploited to close the truncated to 2oMs relations, and develop correlations specific to this class of

very-cold-wall flows (§ 5.2). In § 6, we study briefly the transport equations for the variance and fluxes of h', and discuss their scaling with $(Re_{\tau^\star}, \bar{M}_{CL_x})$. Finally, in § 7, we summarise the conclusions of the present work and discuss possible perspectives for the extension of a correlation-based Reynolds analogy approach to general parallel flows.

2. DNS data

The DNS code (Gerolymos, Sénéchal & Vallet 2009, 2010) used to acquire the data solves the compressible Navier–Stokes equations with perfect gas constant c_p thermodynamics, for which the fluctuations of enthalpy h' are proportional to the fluctuations of temperature T':

$$\left.\begin{aligned} p &= \rho R_g T, \\ c_p &= \frac{\gamma}{\gamma-1} R_g \end{aligned}\right\} \implies \begin{cases} h' = c_p\, T', \\ a = \sqrt{\gamma R_g T}, \end{cases} \tag{2.1}$$

where $R_g = 287.04\ \mathrm{m^2\ s^{-2}\ K^{-1}}$ is the gas constant for air, $\gamma = 1.4$ is the isentropic exponent for air, c_p is the heat capacity at constant pressure, p is the pressure, ρ is the density, T is the temperature, and a is the sound velocity. Linear molecular constitutive relations are used for the viscous stresses and heat fluxes, with $\mu_b = 0$ bulk viscosity, and Sutherland laws for the dynamic viscosity $\mu(T)$ and the heat conductivity $\lambda(T)$ (Gerolymos 1990).

Following Coleman *et al.* (1995), the TPC flow computations apply constant wall temperature $T_w = \text{const.}$ for all t, and bulk density $\rho_B := (\iiint_{\mathfrak{B}} \rho \,\mathrm{d}x\,\mathrm{d}y\,\mathrm{d}z)/\,|\mathfrak{B}| = \text{const.}$ for all t (Gerolymos *et al.* 2010, (47), p. 791), and adjust the body acceleration f_{V_x} at every subiteration to obtain at statistical convergence of the computations a target bulk mass flow (Gerolymos *et al.* 2010, (48), p. 791), which as ρ_B is constant is tantamount to applying a target-mass-averaged bulk velocity $\overline{u_B} = \overline{(\rho u)_B}/\rho_B$ (table 1).

Although the above conditions fix for each computation the target bulk Mach number M_{B_w} and bulk Reynolds number Re_{B_w} (table 1), these parameters were chosen carefully during the construction of the database (Gerolymos & Vallet 2023) to obtain systematic variation of the Huang–Coleman–Bradshaw (HCB) friction Reynolds number $Re_{\tau^\star}$ (Huang *et al.* 1995) and the streamwise centreline Mach number $\bar{M}_{CL_x}$:

$$\left.\begin{aligned} \bar{M}_{CL_x} &:= \overline{\left(\frac{u_{CL}}{a_{CL}}\right)}, && 0.3 \lessapprox \bar{M}_{CL_x} \lessapprox 2.49, \\ Re_{\tau^\star} &:= \frac{\bar{\rho}_{CL}}{\bar{\mu}_{CL}}\sqrt{\frac{\bar{\tau}_w}{\bar{\rho}_{CL}}}\,\delta, && 100 \lessapprox Re_{\tau^\star} \lessapprox 1000, \end{aligned}\right\} \tag{2.2}$$

instead, as these parameters (2.2) are more generally relevant, especially with regard to TBLs. The computational box size was $L_x \times L_y \times L_z = 8\pi\delta \times 2\delta \times 4\pi\delta$, where $\{x, y, z\}$ are the {streamwise, wall-normal, spanwise} Cartesian coordinates (the lower wall is located at $y = 0$) with corresponding velocity components $\{u, v, w\}$. Details on computational resolution and statistics sampling frequency and interval were reported in Gerolymos & Vallet (2023, table 1, p. A19-8). Results with the DNS solver used (statistics for moments of order 2 and 3, budgets for Reynolds stresses and their dissipation tensor, spectra) have been validated systematically by comparison with other available DNS data (Gerolymos *et al.* 2010; Gerolymos, Sénéchal & Vallet 2013; Gerolymos & Vallet 2016).

https://doi.org/10.1017/jfm.2023.1034 Published online by Cambridge University Press

$L_x \times L_y \times L_z = 8\pi\delta \times 2\delta \times 4\pi\delta$; $T_w = 298$ K = const.; $Pr_w = 0.7063$

$Re_{\tau^\star}$	$\bar{M}_{CL_x}$	Re_{τ_w}	$Re_{\theta_{CL}}$	Re_{B_w}	M_{B_w}	$\frac{\overline{u_B}}{\bar{u}_{CL}}$	B_{q_w}	$\frac{\overline{T_B}}{\bar{T}_w}$	$\frac{\bar{T}_{CL}}{\bar{T}_w}$	$\frac{T_r}{\bar{T}_w}$	$\frac{\bar{h}_{CL}-\bar{h}_w}{\frac{1}{2}\bar{u}_{CL}^2}$	$\frac{1}{\bar{u}_{CL}}\frac{\mathrm{d}\bar{h}}{\mathrm{d}\bar{u}}\Big\vert_w$
66.1	1.627	101.9	130.6	1301.0	1.506	0.7778	−0.052123	1.36117	1.41717	2.085	0.5561	0.5490
73.7	0.329	74.9	125.1	1054.6	0.266	0.8029	−0.001980	1.01124	1.01274	1.032	0.5827	0.5672
73.9	0.806	81.6	127.4	1128.9	0.672	0.8019	−0.012172	1.07193	1.08158	1.207	0.5807	0.5663
77.3	1.495	112.5	135.1	1458.4	1.398	0.8046	−0.045922	1.30958	1.35054	1.888	0.5809	0.5682
75.1	2.054	165.7	138.5	1869.3	2.263	0.7955	−0.100397	1.80401	1.91734	3.357	0.5668	0.5618
102.7	1.506	153.0	165.9	2016.3	1.471	0.8327	−0.048866	1.34102	1.37708	1.933	0.6038	0.5880
100.3	1.819	186.0	168.0	2308.0	1.934	0.8271	−0.075692	1.58750	1.65285	2.626	0.5969	0.5840
100.4	1.918	203.0	169.8	2428.2	2.113	0.8264	−0.087508	1.69952	1.77754	2.941	0.5948	0.5836
98.9	2.015	218.7	169.7	2545.1	2.299	0.8238	−0.099097	1.82513	1.91932	3.306	0.5900	0.5814
97.3	2.110	237.7	170.2	2674.2	2.504	0.8202	−0.112260	1.97739	2.09254	3.751	0.5863	0.5793
98.5	2.218	275.7	170.3	2920.1	2.795	0.8211	−0.132763	2.21288	2.35558	4.418	0.5850	0.5802
104.8	0.324	106.5	161.4	1550.7	0.273	0.8371	−0.002024	1.01180	1.01299	1.032	0.6106	0.5912
106.0	0.793	117.3	165.3	1678.6	0.691	0.8375	−0.012406	1.07555	1.08313	1.204	0.6101	0.5916
113.7	1.507	169.9	182.0	2259.5	1.487	0.8393	−0.049172	1.34768	1.38187	1.940	0.6085	0.5927
111.7	2.020	252.1	191.3	2947.8	2.350	0.8323	−0.100937	1.86254	1.95334	3.372	0.5979	0.5877
112.7	2.488	490.6	199.7	4438.9	3.838	0.8249	−0.199724	3.24087	3.49627	7.349	0.5766	0.5825
134.2	1.991	297.9	223.4	3521.0	2.330	0.8434	−0.098938	1.84761	1.92569	3.285	0.6063	0.5958
143.1	0.324	145.5	220.8	2196.6	0.278	0.8520	−0.002020	1.01222	1.01323	1.032	0.6220	0.6017
151.4	0.792	167.8	236.9	2507.7	0.705	0.8543	−0.012313	1.07854	1.08484	1.206	0.6235	0.6034
151.5	1.503	227.6	245.3	3100.2	1.508	0.8519	−0.048970	1.35765	1.38696	1.944	0.6178	0.6016
168.7	0.793	187.2	269.1	2829.3	0.708	0.8569	−0.012286	1.07942	1.08544	1.207	0.6252	0.6053
176.6	0.347	180.0	279.4	2785.6	0.300	0.8581	−0.002295	1.01428	1.01532	1.037	0.6263	0.6060
251.1	0.828	281.6	424.0	4479.2	0.749	0.8650	−0.012940	1.08915	1.09472	1.228	0.6314	0.6109
253.9	1.471	377.0	438.5	5468.2	1.490	0.8641	−0.045106	1.35134	1.37348	1.903	0.6282	0.6104
245.3	1.988	554.6	435.7	6909.3	2.395	0.8611	−0.096300	1.89781	1.95708	3.334	0.6187	0.6079
339.6	0.798	378.0	594.0	6266.2	0.724	0.8705	−0.011663	1.08356	1.08814	1.211	0.6367	0.6147
341.8	1.513	522.9	615.4	7813.2	1.560	0.8691	−0.046795	1.38636	1.40787	1.982	0.6327	0.6138
341.0	1.978	767.8	634.2	9961.8	2.393	0.8666	−0.092221	1.89904	1.95021	3.308	0.6229	0.6115
984.5	0.806	1100.5	1935.0	21091.7	0.743	0.8831	−0.010558	1.08856	1.09198	1.218	0.6489	0.6223
965.2	1.505	1479.0	1947.5	25215.9	1.575	0.8811	−0.041396	1.39476	1.41016	1.979	0.6421	0.6204

Table 1. Parameters of the DNS computations, where: L_x, L_y, L_z are the dimensions of the computational domain (directions x = homogeneous streamwise, y = wall-normal, z = homogeneous spanwise); u, v, w are are the velocity components along x, y, z; δ is the channel half-height; $(\cdot)_w$ denotes wall values and $(\cdot)_{CL}$ centreline values; $(\cdot)_B$ denotes bulk (volume) averages; $\rho_B := (\int_0^\delta \bar{\rho}\,\mathrm{d}y)/\delta = \text{const.}$; $\overline{u_B} := \overline{(\rho u)_B}/\rho_B = (\int_0^\delta \bar{\rho}\tilde{u}\,\mathrm{d}y)/(\delta\rho_B)$; $\overline{T_B} := \overline{(\rho T)_B}/\rho_B = (\int_0^\delta \bar{\rho}\tilde{T}\,\mathrm{d}y)/(\delta\rho_B)$; $Re_{\tau^\star} := \sqrt{(\bar{\rho}_{CL}\bar{\tau}_w)}\delta/\bar{\mu}_{CL}$ is the friction Reynolds number in Huang–Coleman–Bradshaw scaling; $\bar{M}_{CL_x} := \overline{u_{CL}/a_{CL}}$ is the centreline Mach number; $Re_{\tau_w} := \bar{\rho}_w u_\tau \delta/\bar{\mu}_w$ is the friction Reynolds number; $u_\tau := \sqrt{(\bar{\tau}_w/\bar{\rho}_w)}$ is the friction velocity; $Re_{\theta_{CL}} := \bar{\rho}_{CL}\tilde{u}_{CL}\theta/\bar{\mu}_{CL}$ is the momentum-thickness Reynolds number at centreline conditions; $\theta := \int_0^\delta (1-\tilde{u}/\tilde{u}_{CL})\overline{\rho u}/\overline{\rho u}_{CL}\,\mathrm{d}y$ is the momentum thickness; $Re_{B_w} := \rho_B \overline{u_B}\delta/\bar{\mu}_w$ is the bulk Reynolds number; $M_{B_w} := \overline{u_B}/\bar{a}_w$ is the bulk Mach number at wall sound speed; T_r is the theoretical adiabatic wall temperature ($h_r := \bar{h}_{CL} + \frac{1}{2} r_f \bar{u}_{CL}^2$, $r_f = 0.89$); $B_{q_w} := \bar{q}_w/(\bar{\rho}_w u_\tau \bar{c}_{p_w} \bar{T}_w)$ is the non-dimensional wall heat flux (Coleman *et al.* 1995); and $(\bar{h}_{CL} - \bar{h}_w)/(\frac{1}{2}\bar{u}_{CL}^2)$ and $(d_{\tilde{u}}\bar{h})|_w/\bar{u}_{CL}$ are the non-dimensional enthalpy rise and the wall heat flux parameter.

The present data on mean and fluctuating temperature are in very good agreement with available data in the databases of Modesti & Pirozzoli (2016) and Yao & Hussain (2020). The consistency of the statistical convergence of the computations is examined and compared with other DNS data in § 3.3. Relevant h'_t statistics and p.d.f.s were acquired directly, with sampling at every computational time step. All moments present in the exact relations (1.1) were also acquired, and the budgets of (1.1) were checked to verify convergence of the statistics.

Following (Huang *et al.* 1995), inner scaling was based on the system of units defined by

$$(\cdot)^\star - \text{units} : \{\bar\tau_w, \bar\rho(y), \bar\mu(y)\}, \tag{2.3}$$

following accepted practice in compressible wall turbulence (Trettel & Larsson 2016), and were plotted against

$$y^\star := \frac{\bar\rho(y)\sqrt{\dfrac{\bar\tau_w}{\bar\rho(y)}}\,y}{\bar\mu(y)}. \tag{2.4}$$

It should be stressed here that when presenting terms including derivatives in $(\cdot)^\star$ units, there is no transformation of the variables implied or used, but simply the term is made non-dimensional in $(\cdot)^\star$ units.

3. Frictional heating and mean enthalpy

Before analysing the h'_t and h' correlations, it is useful to identify the parameters characterising the thermal turbulence structure (§ 3.1) and to verify the consistency and accuracy of the computations (§ 3.3).

3.1. *Frictional heating*

The mean flow equations in the case of steady ($\partial_t\overline{(\cdot)}=0$) streamwise-invariant ($\partial_x\overline{(\cdot)}=0$) compressible TPC ($\partial_z\overline{(\cdot)}=0$) flow between two isothermal walls and equation of state (2.1) read (Huang *et al.* 1995; Gerolymos & Vallet 2014)

$$\overline{\rho v} = \bar\rho\tilde v = 0, \tag{3.1a}$$

$$\frac{\mathrm{d}}{\mathrm{d}y}\left(-\overline{\rho u''v''}+\bar\tau_{xy}\right)+\overline{\rho f_{V_x}}=0 \implies \rho_B\bar f_{V_x}=\frac{\bar\tau_w}{\delta}, \tag{3.1b}$$

$$\frac{\mathrm{d}}{\mathrm{d}y}\left(-\overline{\rho v''h''_t}+\overline{u_i\tau_{iy}}-\bar q_y\right)+\overline{\rho u f_{V_x}}=0 \implies \rho_B\overline{u}_B\bar f_{V_x}=-\frac{\bar q_w}{\delta}, \tag{3.1c}$$

$$\frac{\mathrm{d}}{\mathrm{d}y}\left(-\overline{\rho v''h''}-\bar q_y\right)+\overline{\frac{\mathrm{D}p}{\mathrm{D}t}}+\overline{\tau_{ij}S_{ij}}=0 \overset{(3.2)}{\implies} \bar q_w=-\int_0^\delta\left(\overline{\tau_{ij}S_{ij}}-\overline{p\Theta}\right)\mathrm{d}y, \tag{3.1d}$$

for the continuity (3.1*a*), streamwise (x direction) momentum (3.1*b*), total energy (3.1*c*), and static enthalpy (3.1*d*), respectively. The relations implied in (3.1*b*) and (3.1*c*) are obtained readily by integration across the channel (Huang *et al.* 1995), using the fact that the body acceleration f_{V_x} does not vary in space but only in time, and for (3.1*c*) that $\rho_B=$ const. for all t. They are satisfied upon statistical convergence of the averages.

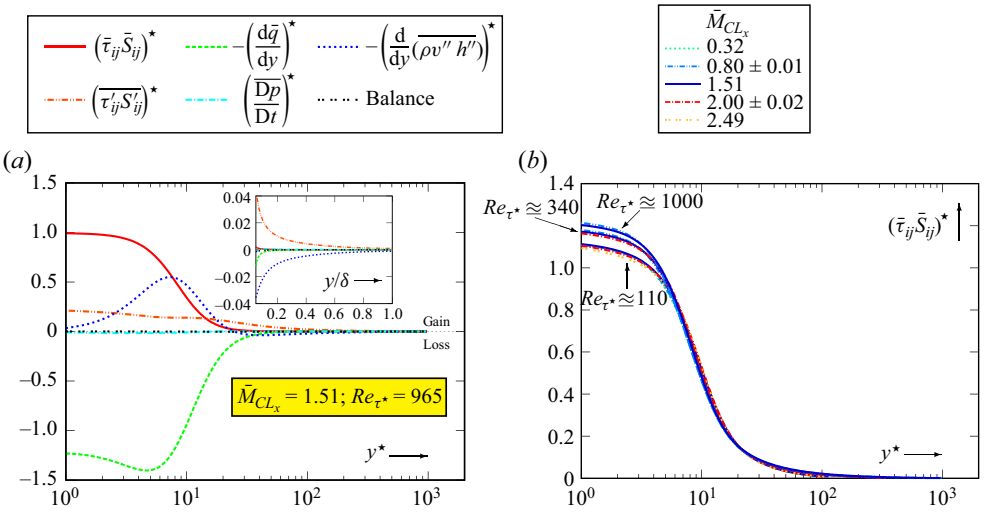

Figure 1. (*a*) Budgets of the static enthalpy (temperature) (3.1*d*), in $(\cdot)^\star$ units, plotted against $y^\star$ (log scale), with an outer region zoom plotted against y/δ (linear), at $(Re_{\tau^\star}, \bar{M}_{CL_x}) = (965, 1.51)$. (*b*) Frictional heat generation term $\overline{\tau_{ij}S_{ij}}^\star$ for varying $0.32 \leq \bar{M}_{CL_x} \leq 2.49$ at nearly constant $Re_{\tau^\star} \in \{110, 340, 1000\}$, from the present DNS database (table 1).

To obtain the integral relation implied in (3.1*d*), we also used the flow symmetries to simplify the substantial derivative $\mathrm{D}_t p$:

$$\overline{\frac{\mathrm{D}p}{\mathrm{D}t}} \overset{[\partial_t\overline{(\cdot)}=0]}{=} \overline{u_j \frac{\partial p}{\partial x_j}} = \frac{\partial}{\partial x_j}\left(\overline{pu_j}\right) - \overline{p\Theta} \overset{[\partial_x\overline{(\cdot)}=\partial_z\overline{(\cdot)}=0]}{=} \frac{\mathrm{d}}{\mathrm{d}y}\left(\overline{pv}\right) - \overline{p\Theta}, \tag{3.2}$$

where $\Theta := \partial_{x_j} u_j$ is the dilatation, S_{ij} is the rate of deformation, and τ_{ij} is the viscous stress. This identifies $\overline{\tau_{ij}S_{ij}} \ggg \left|\overline{p\Theta}\right|$ as the heat production mechanism, as is also seen in the budgets (figure 1*a*) of the static enthalpy equation (3.1*d*). Near the wall ($y^\star \lessapprox 5$), $\overline{\tau_{ij}S_{ij}} = \bar{\tau}_{ij}\bar{S}_{ij} + \overline{\tau'_{ij}S'_{ij}}$ is balanced principally by molecular heat conduction $-d_y\bar{q}_y$. Notice that at constant $Re_{\tau^\star}$, near the wall ($y^\star \lessapprox 10$), the heat production term follows $(\cdot)^\star$ scaling with varying Mach number (figure 1*b*), i.e. $\overline{\tau_{ij}S_{ij}}^\star := \overline{\tau_{ij}S_{ij}}/(\bar{\tau}_w^2/\bar{\mu}(y))$ depends essentially on $Re_{\tau^\star}$ and much less on $\bar{M}_{CL_x}$. Above the buffer layer ($y^\star \gtrapprox 60$), and up to the centreline, there is essentially a balance between heat production by the fluctuating field $\overline{\tau'_{ij}S'_{ij}}$ and turbulent mixing $-d_y(\overline{\rho v'' h''})$ (figure 1*a*), whereas the pressure term $\overline{\mathrm{D}_t p}$ is negligible everywhere. Turbulent mixing $-d_y(\overline{\rho v'' h''})$ changes sign at $y^\star \approx 25$, opposing molecular heat conduction and enhancing heating in the near-wall region (figure 1*a*).

3.2. *The $\bar{h}(\bar{u})$ relation*

Usually, mean thermal field relations, for attached wall turbulent flows (Zhang *et al.* 2014, 2017, 2018; Song *et al.* 2022), TPCs or TBLs, are presented in terms of temperature ratio $\bar{T}(y)/\bar{T}_\delta$, which of course depends strongly on the Mach number $\bar{M}_\delta$. This representation misses the point that working instead in terms of non-dimensional enthalpy differences (figure 2), in the TPC case $(\bar{h} - \bar{h}_w)/(\frac{1}{2}\bar{u}_{CL}^2)$, absorbs the largest part of the

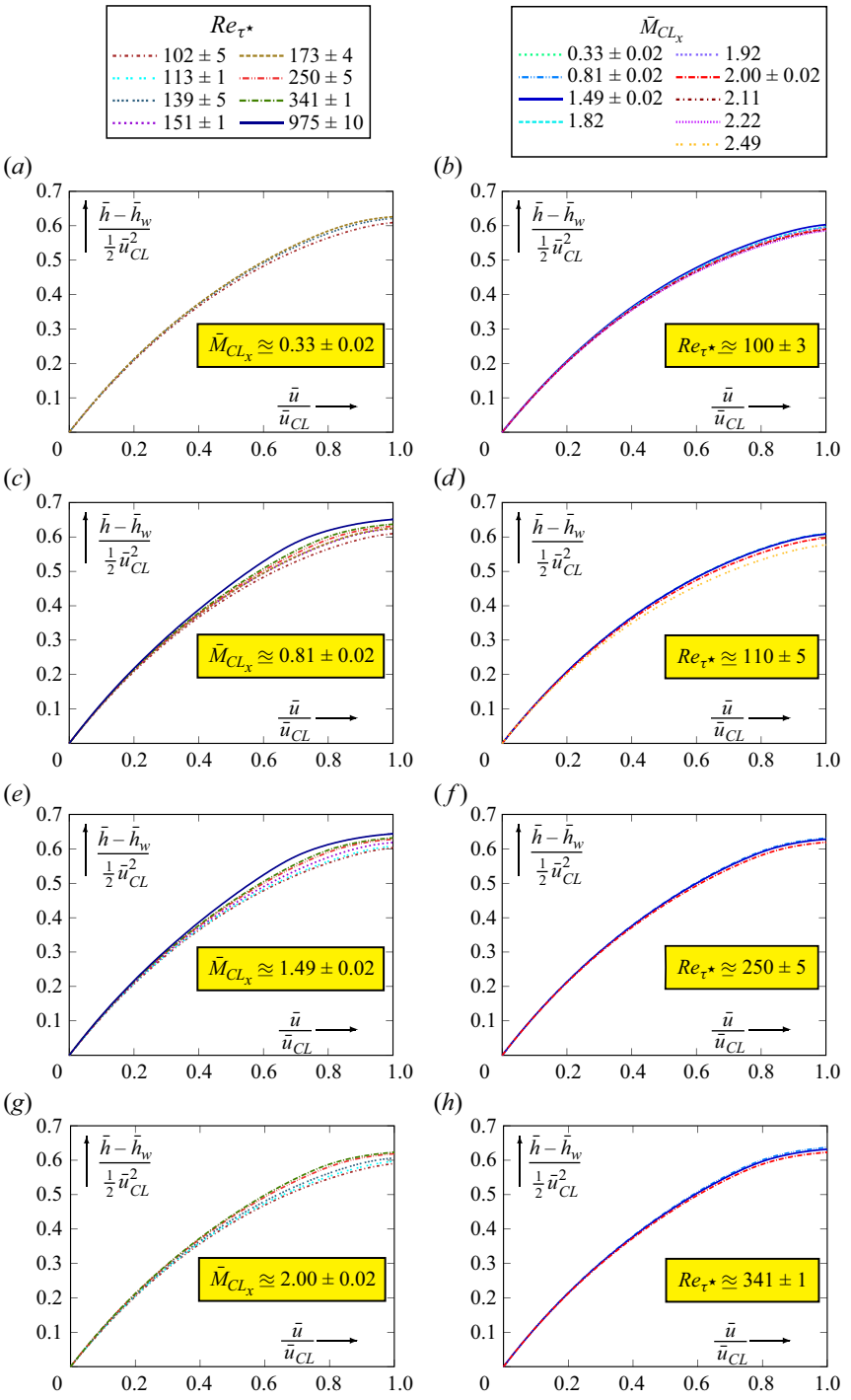

Figure 2. Non-dimensional mean enthalpy rise $(\bar{h}-\bar{h}_w)/(\frac{1}{2}\bar{u}_{CL}^2)$ plotted against the non-dimensional velocity $\bar{u}/\bar{u}_{CL}$, for (*a*,*c*,*e*,*g*) varying HCB Reynolds numbers $97 \leq Re_{\tau^\star} \leq 985$ at nearly constant centreline Mach numbers $\bar{M}_{CL_x} \in \{0.33, 0.80, 1.50, 2.00\}$, and (*b*,*d*,*f*,*h*) varying Mach numbers $0.32 \leq \bar{M}_{CL_x} \leq 2.49$ at nearly constant $Re_{\tau^\star} \in \{100, 110, 250, 340\}$, from the present DNS database (table 1).

Mach dependence, results at nearly constant $Re_{\tau\star}$ (figures 2*b*,*d*,*f*,*h*) showing quite weak $\bar{M}_{CL_x}$ dependence, while results at nearly constant $\bar{M}_{CL_x}$ (figures 2*a*,*c*,*e*,*g*) show noticeable $Re_{\tau\star}$ dependence, which is discussed further in § 3.3.

It is generally verified that a quadratic polynomial of streamwise velocity $\bar{u}$ that satisfies the wall heat flux $(d_{\bar{u}}\bar{T})|_w$ and the wall and centreline values of temperature fits reasonably well the DNS data for attached wall turbulent flows (Zhang *et al.* 2017, 2018; Song *et al.* 2022). Using enthalpies instead, it is straightforward to show that the unique one-sided Hermitian quadratic polynomial (Stoer & Bulirsch 1993, p. 53) that satisfies wall and centreline values and wall flux reads

$$\frac{\bar{h}-\bar{h}_w}{\bar{u}_{CL}^2} \approxeq \frac{1}{\bar{u}_{CL}}\left.\frac{\mathrm{d}\bar{h}}{\mathrm{d}\bar{u}}\right|_w \frac{\bar{u}}{\bar{u}_{CL}} + \left(\frac{\bar{h}_{CL}-\bar{h}_w}{\bar{u}_{CL}^2} - \frac{1}{\bar{u}_{CL}}\left.\frac{\mathrm{d}\bar{h}}{\mathrm{d}\bar{u}}\right|_w\right)\left(\frac{\bar{u}}{\bar{u}_{CL}}\right)^2 + \text{approximation error}, \tag{3.3}$$

and this is precisely the polynomial for the non-dimensional temperature obtained using physical Reynolds analogy arguments by Zhang *et al.* (2014). Therefore, to the order of the approximation error, the mean enthalpy field depends on two parameters, namely the non-dimensional wall heat flux $(d_{\bar{u}}\bar{h})|_w/\bar{u}_{CL}$ and the wall-to-centreline enthalpy rise $-r_h := (\bar{h}_{CL}-\bar{h}_w)/(\frac{1}{2}\bar{u}_{CL}^2)$, which in adiabatic wall flows should correspond to the adiabatic recovery factor r_f. The DNS data (table 1) show clearly that both these parameters depend principally on $Re_{\tau\star}$ and only weakly on $\bar{M}_{CL_x}$. It will be seen that all of the flows in the database have very similar turbulence structure (§ 4), therefore they should be characterised not by temperature ratios like $\bar{T}_{CL}/\bar{T}_w$, which depend very strongly on $\bar{M}_{CL_x}$, but by $-r_h$ instead.

3.3. *Consistency check and comparison with available data*

Notice that combining the integral relations for x momentum (3.1*b*) and total energy (3.1*c*) readily relates the wall heat flux $\bar{q}_w$ and the wall shear stress $\bar{\tau}_w$ by the exact relation (Huang *et al.* 1995; Song *et al.* 2022)

$$(3.1b),\,(3.1c) \implies \frac{\bar{q}_w}{\bar{\tau}_w} = -\overline{u_B} \overset{(3.4b)}{\implies} \frac{1}{\bar{u}_{CL}}\left.\frac{\mathrm{d}\bar{h}}{\mathrm{d}\bar{u}}\right|_w \approxeq Pr_w\,\frac{\overline{u_B}}{\bar{u}_{CL}}, \tag{3.4a}$$

where we used

$$-\frac{\bar{q}_w}{\bar{\tau}_w} \approxeq \frac{\bar{\lambda}_w\left.\dfrac{\mathrm{d}\bar{T}}{\mathrm{d}y}\right|_w}{\bar{\mu}_w\left.\dfrac{\mathrm{d}\bar{u}}{\mathrm{d}y}\right|_w} \approxeq \frac{\bar{\lambda}_w\left.\dfrac{\mathrm{d}\bar{h}}{\mathrm{d}y}\right|_w}{\bar{\mu}_w\bar{c}_{p_w}\left.\dfrac{\mathrm{d}\bar{u}}{\mathrm{d}y}\right|_w} \approxeq \frac{1}{\overline{Pr_w}}\left.\frac{\mathrm{d}\bar{h}}{\mathrm{d}\bar{u}}\right|_w. \tag{3.4b}$$

In the case of strictly isothermal walls ($T_w = \text{const.}$) used in the present computations, there are no fluctuations of the molecular transport coefficients or heat capacity at the wall, so (3.4*b*) is exact, and so is the final relation in (3.4*a*).

Checking whether the DNS results satisfy the exact relation (3.4*a*) is a good test in assessing proper convergence of the computations (and statistics) regarding the thermal field. The integral relation (3.1*d*) for the wall heat flux shows that $\bar{q}_w$ is affected by the integration of $\overline{\tau_{ij}S_{ij}}$ across the entire channel, and explains the observed

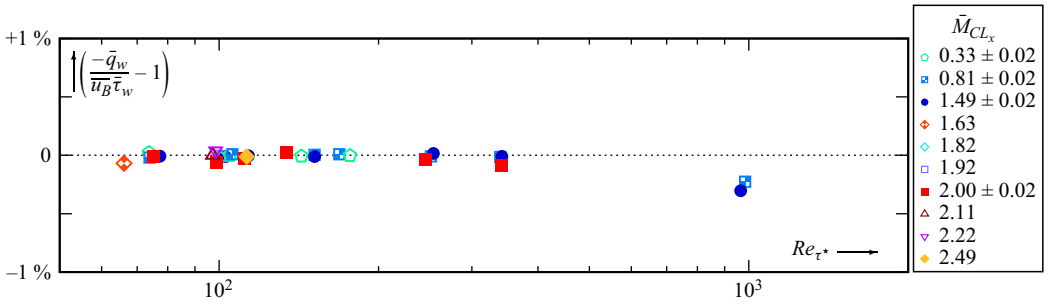

Figure 3. Consistency diagnostic of the present DNS computations (table 1) by verification of the exact (at statistical convergence) relation $\bar{q}_w = -\overline{u_B}\bar{\tau}_w$ (see (3.4*a*)) obtained from the integration of the mean momentum and energy equations across the channel (Huang *et al.* 1995; Song *et al.* 2022), which also provides the heat flux parameter in the quadratic approximation of the $\bar{h}(\bar{u})$ relation (3.3).

slow convergence of centreline temperature $\bar{T}_{CL}$, especially with increasing Reynolds number. The present DNS data satisfy the exact relation (3.4*a*) with accuracy better than $0.25\,\% \equiv 2.5\,‰$ (figure 3).

Regarding the prediction of the centreline-to-wall temperature ratio $\bar{T}_{CL}/\bar{T}_w$ (figure 4*a*), the present data (table 1) are in very good agreement with the DNS data of Modesti & Pirozzoli (2016) and Yao & Hussain (2020) ($Pr = 0.72$), and of Trettel & Larsson (2016), indicating that it increases approximately as

$$\frac{\bar{T}}{\bar{T}_w} \approxeq 1 + (0.17 \pm 0.005) M_{B_w}^2 . \tag{3.5}$$

The small variation of the coefficient in the correlation (3.5) determines the limits of the envelope of the data. These variations in the M_{B_w} dependence around the average curve actually reveal the Re influence on $\bar{T}_{CL}/\bar{T}_w$.

Song *et al.* (2022, (14), p. 6) developed the alternative correlation

$$\frac{\bar{T}}{\bar{T}_w} \approxeq 1 + 1.034\, Pr_w \frac{\bar{u}_{CL}}{\overline{u_B}} M_{B_w}^2 \iff \frac{\bar{h}_{CL} - \bar{h}_w}{\frac{1}{2}\bar{u}_{CL}^2} \approxeq 1.034\, Pr_w \frac{\overline{u_B}}{\bar{u}_{CL}} \tag{3.6}$$

that was rewritten here as (3.6) in terms of the enthalpy rise parameter $-r_h := (\bar{h}_{CL} - \bar{h}_w)/(\frac{1}{2}\bar{u}_{CL}^2)$, showing clearly that r_h in the correlation of Song *et al.* (2022) depends not on M_{B_w}, but on $\overline{u_B}/\bar{u}_{CL}$ instead, which is tantamount to including a Re effect because of the strong sensitivity of the ratio $\overline{u_B}/\bar{u}_{CL}$ on $Re_{\tau^\star}$, especially in this relatively low $Re_{\tau^\star} \lessapprox 1482$ range (table 1). Closer examination of the data (figure 4*b*) reveals that there still exists a slight $\bar{M}_{CL_x}$ sensitivity. The value of the ratio $\overline{u_B}/\bar{u}_{CL}$ used in (3.6) was calculated carefully by integrating (table 1) the density and mass flux profiles in the databases of Modesti & Pirozzoli (2016) and Yao & Hussain (2020), and is slightly different to the values tabulated in Song *et al.* (2022).

The empirical correlation coefficient 1.034 in (3.6) is probably a little too high at the lower Re (lower $\overline{u_B}/\bar{u}_{CL}$) range (figure 4*b*). The data of Yao & Hussain (2020) at the higher $Re_{\tau^\star} \gtrapprox 1000$ ($\overline{u_B}/\bar{u}_{CL} \gtrapprox 0.88$) indicate (figure 4*b*) not only a steepening of the slope but also a crossing between the $\bar{M}_{CL_x} \approxeq 1.46$ and $\bar{M}_{CL_x} \approxeq 0.87$ curves, which was not observed in the present database. This highlights the need for higher Re data to fill the gap with incompressible DNS data, which are currently at $Re_{\tau_w} \approxeq 10\,000$ (Hoyas *et al.* 2022),

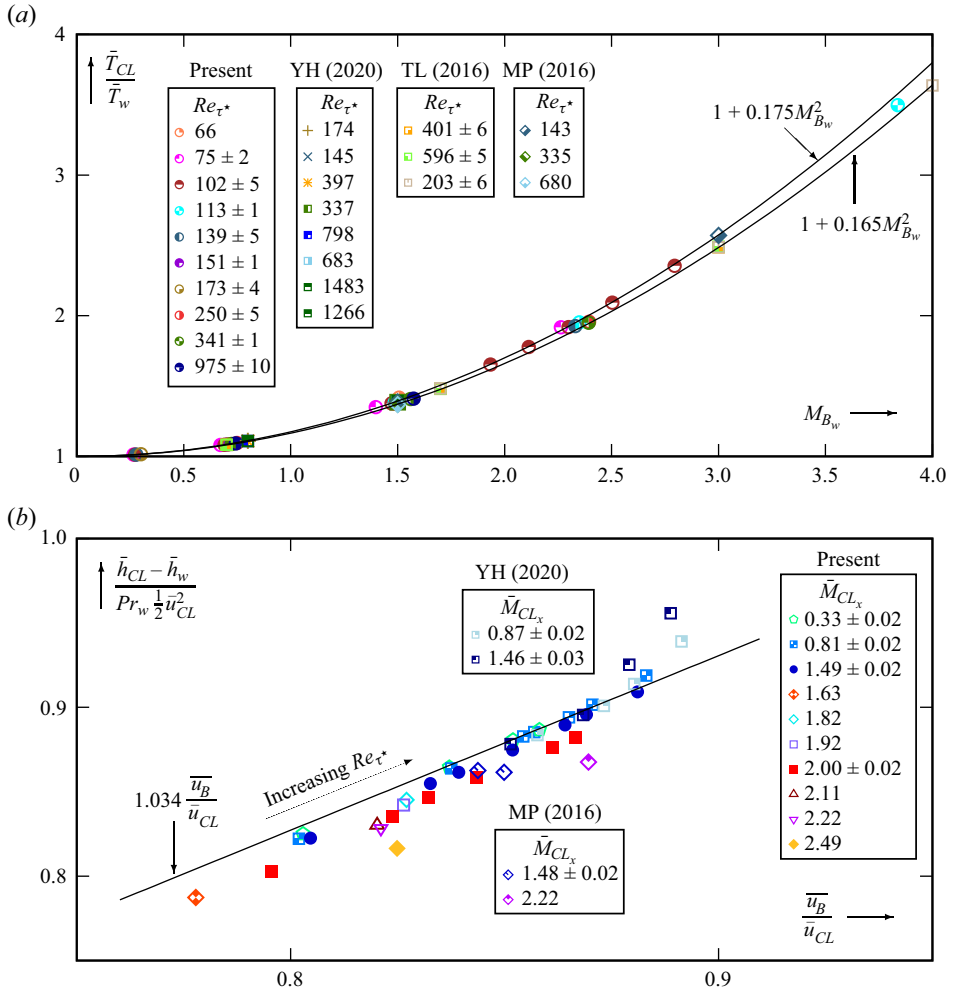

Figure 4. (*a*) Centreline-to-wall temperature ratio versus M_{B_w} and (*b*) non-dimensional enthalpy difference $(\bar{h}_{CL} - \bar{h}_w)/(\frac{1}{2}\,Pr_w\,\bar{u}^2_{CL})$ versus $\overline{u_B}/\bar{u}_{CL}$, for the present DNS data (table 1) and other available DNS data of Modesti & Pirozzoli (2016), Trettel & Larsson (2016) and Yao & Hussain (2020) (respectively denoted MP (2016), TL (2016), YH (2020)), covering the ranges $0.32 \leq \bar{M}_{CL_x} \leq 2.49$ and $97 \leq Re_{\tau^\star} \leq 1482$, and comparison with the correlation envelope (3.5) in (*a*) and the correlation (3.6) of Song *et al.* (2022) in (*b*).

tenfold higher than the compressible databases (Modesti & Pirozzoli 2016; Trettel & Larsson 2016; Yao & Hussain 2020; Gerolymos & Vallet 2014, 2023).

4. The h'_t and h' statistics

DNS data (Huang *et al.* 1995) show that TPC flow without any artificial source term in the energy equation (Yu *et al.* 2020) is a very-cold-wall (VCW) flow, in the sense that

$$\text{VCW:}\quad \frac{\mathrm{d}\bar{T}}{\mathrm{d}y} > 0 \overset{(2.1)}{\Longrightarrow} \frac{\mathrm{d}\bar{h}}{\mathrm{d}y} > 0 \Longrightarrow \frac{\mathrm{d}\bar{h}}{\mathrm{d}\bar{u}} > 0 \Longrightarrow \begin{cases} \overline{h'u'} > 0, \\ \overline{h'v'} < 0, \\ \overline{h'_t u'} > 0, \\ \overline{h'_t v'} < 0, \end{cases} \quad \forall\, y \in]0, \delta[, \quad (4.1)$$

where the usual attached flow change of variables $y = y(\bar{u})$, based on the monotonicity of $\bar{u}(y)$, was made. This relation (4.1) will be used to define VCW conditions, characteristic of the flows investigated in the paper.

For this class of flows, $h'_{t_{rms}} > h'_{rms}$ (§ 4.3), in contrast to adiabatic or isothermal wall conditions (Shahab *et al.* 2011). The study of correlation coefficients (§ 4.4) and joint p.d.f.s (§ 4.5) reveals a very strong positive correlation between h'_t and u' for all y, also verified for higher-order statistics.

We note

$$(\cdot)'_{rms} := \sqrt{\overline{(\cdot)'^2}}, \tag{4.2a}$$

$$c_{(\cdot)'[\cdot]'} := \frac{\overline{(\cdot)'[\cdot]'}}{\sqrt{\overline{(\cdot)'^2}}\sqrt{\overline{[\cdot]'^2}}} \equiv \frac{\overline{(\cdot)'[\cdot]'}}{(\cdot)'_{rms}\,[\cdot]'_{rms}} \in [-1,\,1], \tag{4.2b}$$

i.e. the r.m.s. of $(\cdot)'$ and the correlation coefficient (CC) between the fluctuations of two flow quantities $[\cdot]'$ and $(\cdot)'$.

4.1. *Exact and truncated relations in nearly parallel flow*

The general expressions (1.1), under the simplification of parallel ($\bar{v} = 0$) or nearly parallel ($|\bar{v}| \lll \bar{u}$) two-dimensional ($\bar{w} = 0$) flow lead to the usual shear flow Reynolds analogies (Huang *et al.* 1995), i.e. the evaluation of thermal (h') correlations from velocity correlations and the mean velocity and enthalpy profiles.

The TPC flow is almost exactly parallel in the mean ($\tilde{v} = 0 \Rightarrow \bar{v} = \overline{v''} \lll \bar{u}\,\forall y > 0$), so the exact relations for h'_t and its correlations simplify to the parallel flow relations

$$\bar{h}_t = \bar{h} + \tfrac{1}{2}\bar{u}^2 + \tfrac{1}{2}\overline{u'_j u'_j}, \tag{4.3a}$$

$$h'_t = h' + \bar{u}\,u' + \tfrac{1}{2}\left(u'_j u'_j - \overline{u'_j u'_j}\right), \tag{4.3b}$$

$$\overline{h'_t u'} = \overline{h'u'} + \bar{u}\,\overline{u'^2} + \tfrac{1}{2}\overline{u'_j u'_j u'}, \tag{4.3c}$$

$$\overline{h'_t v'} = \overline{h'v'} + \bar{u}\,\overline{u'v'} + \tfrac{1}{2}\overline{u'_j u'_j v'}, \tag{4.3d}$$

$$\overline{h'^2} = \overline{h'^2_t} + \overline{u'^2}\,\bar{u}^2 - 2\overline{h'_t u'}\bar{u} - \left(\overline{h'_t u'_j u'_j} - \bar{u}\overline{u'_j u'_j u'}\right) + \tfrac{1}{4}\left(\overline{u'_i u'_i u'_j u'_j} - \overline{u'_i u'_i}\;\overline{u'_j u'_j}\right), \tag{4.3e}$$

$$= \overline{h'^2_t} - \overline{u'^2}\,\bar{u}^2 - 2\overline{h'u'}\bar{u} - \left(\overline{h'u'_j u'_j} + \bar{u}\overline{u'_j u'_j u'}\right) - \tfrac{1}{4}\left(\overline{u'_i u'_i u'_j u'_j} - \overline{u'_i u'_i}\;\overline{u'_j u'_j}\right). \tag{4.3f}$$

As usual, these relations can be simplified further by omitting HoMs, to write approximately

$$\bar{h}_t \approxeq \bar{h} + \tfrac{1}{2}\bar{u}^2 + \text{HoMs} \tag{4.4}$$

for the mean flow, and

$$\overline{h'_t u'} \approxeq \overline{h'u'} + \bar{u}\,\overline{u'^2} + \text{HoMs}, \tag{4.5a}$$

$$\overline{h'_t v'} \approxeq \overline{h'v'} + \bar{u}\,\overline{u'v'} + \text{HoMs}, \tag{4.5b}$$

$$\overline{h'^2} \approxeq \overline{h'^2_t} + \overline{u'^2}\,\bar{u}^2 - 2\overline{h'_t u'}\bar{u} + \text{HoMs}, \tag{4.5c}$$

$$\overline{h'^2_t} \approxeq \overline{h'^2} + \overline{u'^2}\,\bar{u}^2 + 2\overline{h'u'}\bar{u} + \text{HoMs}, \tag{4.5d}$$

for 2oMs. In the following, we will refer to relations (4.5) and to relations that are derived directly from these as truncated-to-2oMs. The HoMs are not always negligibly small, especially near the peaks of the correlation profiles, and also near the centreline (wake region), but (4.4) does remain a satisfactory working approximation to analyse relations between fluctuation amplitudes and CCs, and is the starting point for the development of Reynolds analogies. Introducing CCs

$$c_{h'u'} := \frac{\overline{h'u'}}{h'_{rms}\,u'_{rms}}, \quad c_{h'_t u'} := \frac{\overline{h'_t u'}}{h'_{t_{rms}}\,u'_{rms}}, \tag{4.6a}$$

$$c_{h'v'} := \frac{\overline{h'v'}}{h'_{rms}\,v'_{rms}}, \quad c_{h'_t v'} := \frac{\overline{h'_t v'}}{h'_{t_{rms}}\,v'_{rms}}, \quad c_{u'v'} := \frac{\overline{u'v'}}{u'_{rms}\,v'_{rms}} \tag{4.6b}$$

to replace the corresponding correlations, we may rewrite the working relations (4.5) as

$$(4.5a) \iff c_{h'_t u'}\,h'_{t_{rms}} \approxeq c_{h'u'}\,h'_{rms} + \bar{u}\,u'_{rms}, \tag{4.7a}$$

$$(4.5b) \iff c_{h'_t v'}\,h'_{t_{rms}} \approxeq c_{h'v'}\,h'_{rms} + c_{u'v'}\,\bar{u}\,u'_{rms}, \tag{4.7b}$$

$$(4.5c) \iff \overline{h'^2} \approxeq \overline{h'^2_t} + \overline{u'^2}\,\bar{u}^2 - 2c_{h'_t u'}\,h'_{t_{rms}}\,\bar{u}\,u'_{rms}, \tag{4.7c}$$

$$(4.5d) \iff \overline{h'^2_t} \approxeq \overline{h'^2} + \overline{u'^2}\,\bar{u}^2 + 2c_{h'u'}\,h'_{rms}\,\bar{u}\,u'_{rms}. \tag{4.7d}$$

These relations readily provide a weak Reynolds analogy, based on CCs (Gaviglio 1987). Notice that (4.7*c*) was reported in Gaviglio (1987, (27), p. 915). The truncated-to-2oMs relations (4.7*c*) and (4.7*d*) are not strictly equivalent, because the HoMs neglected in each of them are different.

4.2. *Wall-normal transport and turbulent Prandtl numbers*

In nearly parallel flow, the ratio $\overline{h'v'}/\overline{u'v'}$, between wall-normal transport of temperature and streamwise velocity, is related directly to the turbulent Prandtl number

$$Pr_T := \frac{\overline{\rho u'' v''}}{\overline{\rho h'' v''}}\frac{\mathrm{d}\tilde{h}}{\mathrm{d}y}\frac{\mathrm{d}\tilde{u}}{\mathrm{d}y} = \frac{\widetilde{u'' v''}}{\widetilde{h'' v''}}\frac{\mathrm{d}\tilde{h}}{\mathrm{d}y}\frac{\mathrm{d}\tilde{u}}{\mathrm{d}y}. \tag{4.8}$$

Except in the near-wall region ($y^\star \lessapprox 10$), there is little influence of $\bar{M}_{CL_x}$ on Pr_T (figure 5), data for varying $\bar{M}_{CL_x}$ at nearly constant $Re_{\tau^\star}$ practically collapsing on a single curve, against both inner-scaled $y^\star$ (figures 5*c*,*g*,*k*,*o*) and outer-scaled y/δ wall distance (figures 5*d*,*h*,*l*,*p*). In contrast, $Re_{\tau^\star}$ has a strong influence on Pr_T. At $Re_{\tau^\star} \approxeq 1000$ ($\bar{M}_{CL_x} \in \{0.81, 1.51\}$), as the log region emerges in the mean velocity profile (Krogstad & Torbergsen 2000; Lee & Moser 2015; Hoyas *et al.* 2022), the $Pr_T(y/\delta)$ profile changes substantially in the range $0.2\delta \lessapprox y \lessapprox 0.5\delta$, compared to lower-$Re$ data (figures 5*f*,*j*).

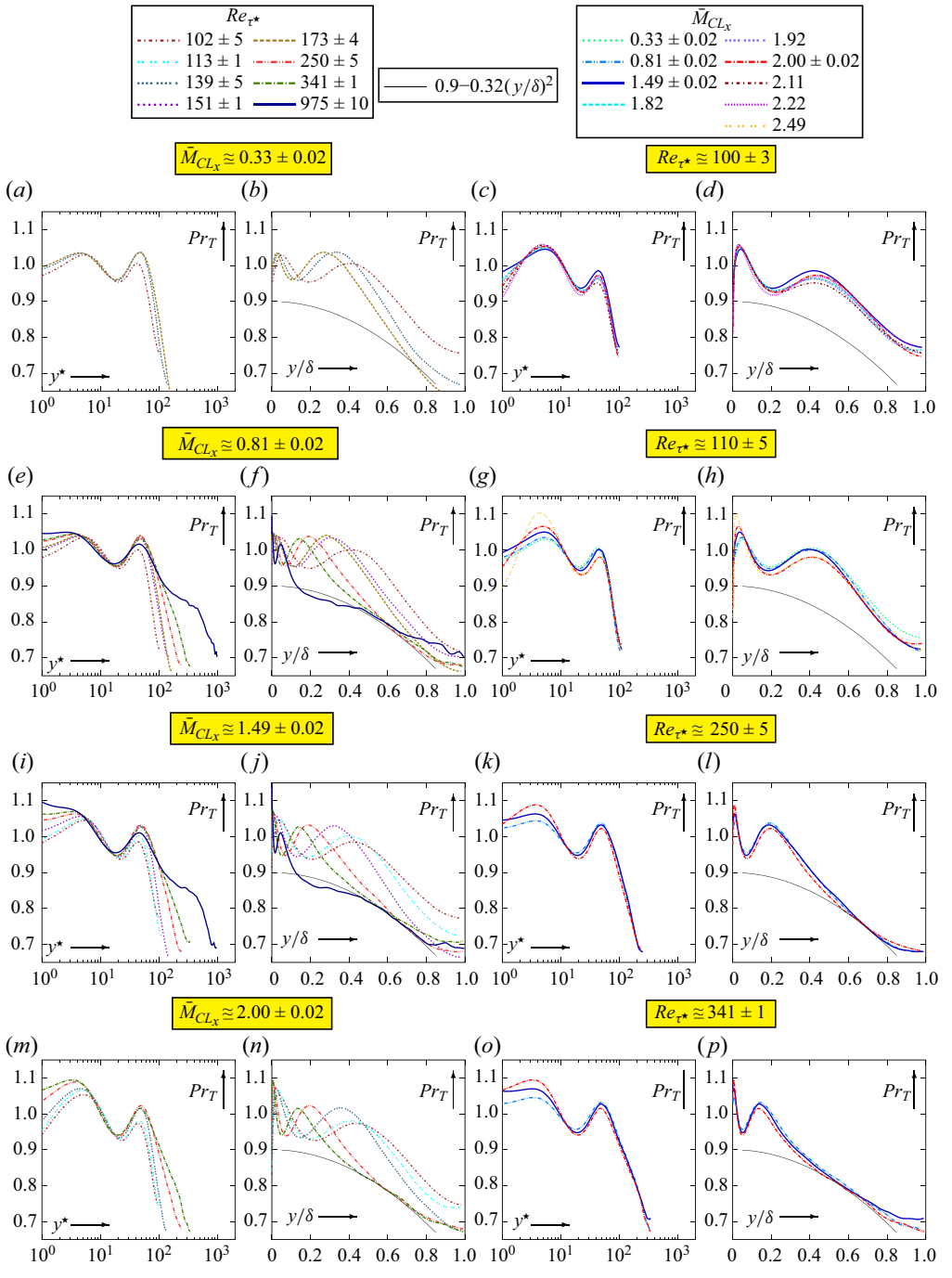

Figure 5. Turbulent Prandtl number Pr_T (4.8), plotted against inner-scaled ($y^\star$, log scale) and outer-scaled (y/δ, linear) wall distance, for varying HCB Reynolds numbers $97 \leq Re_{\tau^\star} \leq 985$ at nearly constant centreline Mach numbers $\bar{M}_{CL_x} \in \{0.33, 0.80, 1.50, 2.00\}$, and for varying $0.32 \leq \bar{M}_{CL_x} \leq 2.49$ at nearly constant $Re_{\tau^\star} \in \{100, 110, 250, 340\}$, from the present DNS database (table 1).

For $Re_{\tau^\star} \gtrapprox 250$, the outer part of the flow seems to follow a consistent outer law

$$Re_{\tau^\star} \gtrapprox 250 \implies \begin{cases} Pr_T \approxeq 0.9 - 0.32\left(\dfrac{y}{\delta}\right)^2, & 0.5\delta \lessapprox y \lessapprox 0.8\delta, \\ Pr_T \approxeq 0.7, & 0.8\delta \lessapprox y, \end{cases} \tag{4.9}$$

similar to the relation proposed (from limited data and based on indirect assessment) by Rotta (1964); the present DNS data (figures 5*b*,*f*,*j*,*n*) suggest a different constant, 0.32, in lieu of 0.4 in Rotta (1964). For the higher $Re_{\tau^\star} \approxeq 1000$, as the buffer region shrinks closer to the wall in the outer-scaled y/δ profiles (figures 5*f*,*j*), the data nearer to the wall ($0.2\delta \lessapprox y \lessapprox 0.5\delta$) are slightly lower than (4.9). Additional DNS data at higher $Re_{\tau^\star}$ are needed to determine the asymptotic high-*Re* form of the outer law, eventually modifying both constants in (4.9) to fit a larger y/δ range. The buffer region seems to follow an inner-scaled profile (figures 5*a*,*e*,*i*,*m*), but higher $Re_{\tau^\star}$ data are required to ascertain the high-*Re* asymptotics of the peak observed at $40 \lessapprox y^\star \lessapprox 45$ and of the valley observed at $17 \lessapprox y^\star \lessapprox 23$ (figures 5*a*,*e*,*i*,*m*). Finally in the near-wall region ($y^\star \lessapprox 10$), Pr_T shows a complex dependence on both $Re_{\tau^\star}$ and $\bar{M}_{CL_x}$ (figure 5).

In lieu of the above usual definition based on Favre averages (4.8), it is the ratio of Reynolds-averaged transport that appears in (4.7*b*), i.e.

$$Pr_{h'} := \frac{\overline{u'v'}}{\overline{h'v'}} \frac{\mathrm{d}\bar{h}}{\mathrm{d}\bar{u}} \equiv \frac{\overline{u'v'}}{\overline{h'v'}} \frac{\mathrm{d}\bar{h}}{\mathrm{d}\bar{u}}, \tag{4.10}$$

where the attached flow transformation $y = y(\bar{u})$ was used. Generally, $Pr_{h'}$ differs very little from Pr_T (figure 6), even for the highest available $\bar{M}_{CL_x} = 2.49$ (figure 6*f*), and this is true for the entire database. Very small differences are observed only around the buffer-region valley (figure 6) which occurs close to the peak of the streamwise Reynolds stress $\overline{\rho u'' u''}$.

Introducing CCs (4.6*b*) in the definition of $Pr_{h'}$ (4.10) yields readily an exact expression for h'_{rms},

$$h'_{rms} \overset{(4.6b),\,(4.10)}{=} \left| \frac{c_{u'v'}}{c_{h'v'}} \frac{1}{Pr_{h'}} \frac{\mathrm{d}\bar{h}}{\mathrm{d}\bar{u}} \right| u'_{rms}, \tag{4.11a}$$

which, combined with the truncated-to-2oMs wall-normal transport relation (4.7*b*), yields an approximate expression for $h'_{t_{rms}}$,

$$h'_{t_{rms}} \overset{(4.5b),\,(4.10)}{\approxeq} \left| \frac{c_{u'v'}}{c_{h'_t v'}} \left(\frac{1}{Pr_{h'}} \frac{\mathrm{d}\bar{h}}{\mathrm{d}\bar{u}} + \bar{u} \right) \right| u'_{rms} + \mathrm{HoMs}, \tag{4.11b}$$

which forms a weak Reynolds analogy, based on the knowledge of the ratios of the wall-normal transport CCs ($c_{u'v'}/c_{h'v'}$, $c_{u'v'}/c_{h'_t v'}$) and of the Prandtl number $Pr_{h'}$.

4.3. *Fluctuation intensities*

Outer-scaling $h'_{t_{rms}}$ or h'_{rms} by $\bar{u}^2_{CL}$ is very successful in accounting for $\bar{M}_{CL_x}$ effects (figures 7*d*,*h*,*l*,*p*), collapsing data for varying $\bar{M}_{CL_x}$ at nearly constant $Re_{\tau^\star}$, except for the near-wall ($y^\star \lessapprox 20$) region (figures 7*c*,*g*,*k*,*o*).

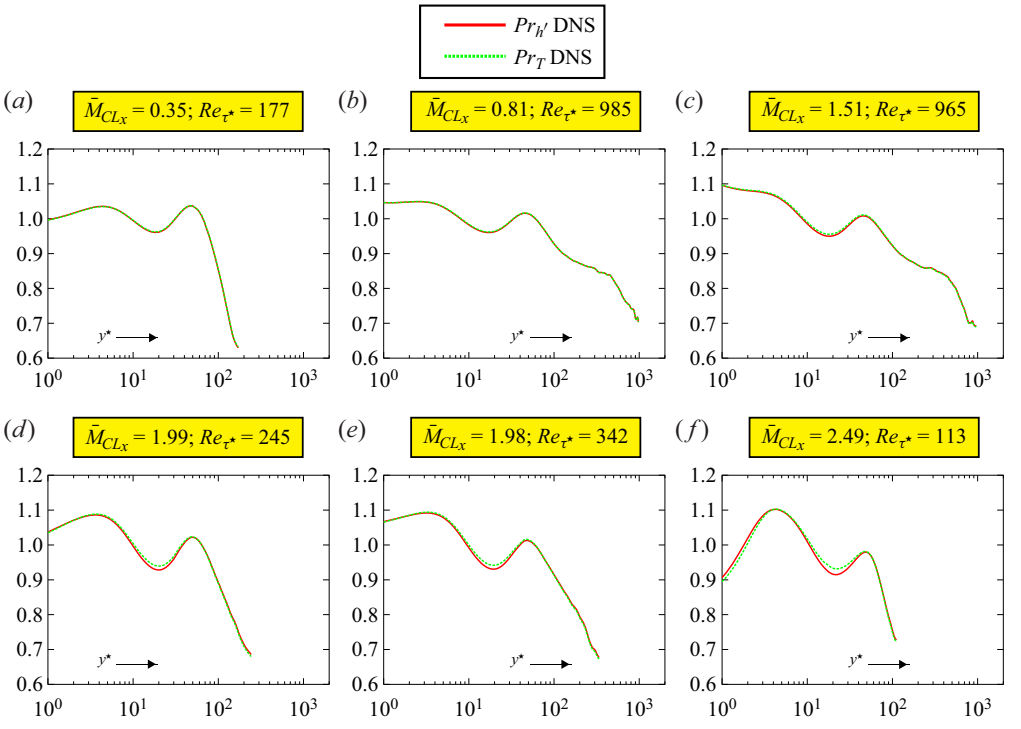

Figure 6. Comparison of turbulent Prandtl numbers Pr_T (4.8) using Favre averages, and $Pr_{h'}$ (4.10) using Reynolds averages, plotted against inner-scaled wall distance $y^\star$ (log scale), for selected flows in the database (table 1), covering the ranges $113 \leq Re_{\tau^\star} \leq 985$ and $0.35 \leq \bar{M}_{CL_x} \leq 2.49$.

On the other hand, there are important differences in $Re_{\tau^\star}$ scaling between $h'_{t_{rms}}$ and h'_{rms}. The peak of $h'_{rms}/\bar{u}^2_{CL}$ reaches an asymptotic level, confirmed by the highest $Re_{\tau^\star} \approxeq 1000$ ($\bar{M}_{CL_x} \in \{0.81, 1.51\}$) data (figures 7*e*,*i*). In contrast, the peak of $h'_{t_{rms}}/\bar{u}^2_{CL}$ decreases with increasing $Re_{\tau^\star}$, suggesting a different inner scaling for $h'_{t_{rms}}$ (figures 7*e*,*i*). The most important difference is observed for the higher available $Re_{\tau^\star} \approxeq 1000$ data, where $h'_{t_{rms}}$ starts forming a plateau in the range $100 \lessapprox y^\star \lessapprox 400$ (figures 7*e*,*i*), suggesting an asymptotic high-Re form. The centreline intensity of $h'_{t_{rms}}/\bar{u}^2_{CL}$ also seems to reach an asymptotic level $\sim$0.04. In contrast, h'_{rms} does not follow this trend, but instead decays continuously from peak to centreline (figures 7*b*,*f*,*j*,*n*), to much lower levels than $h'_{t_{rms}}$. As a consequence, the ratio $h'_{t_{rms}}/h'_{rms} = T'_{t_{rms}}/T'_{rms}$ increases from 1 at the wall (where $u_i = 0$ by the no-slip condition) to quite high values at the centreline (figure 8). The $h'_{t_{rms}}/h'_{rms}$ data at nearly constant $Re_{\tau^\star}$ (figures 8*d*,*h*,*l*,*p*) show very weak $\bar{M}_{CL_x}$ influence, in contrast with data at nearly constant $\bar{M}_{CL_x}$ (figures 8*b*,*f*,*j*,*n*), which show, in the outer part of the flow ($y \gtrapprox \frac{1}{2}\delta$), noticeable increase of the ratio $h'_{t_{rms}}/h'_{rms}$ with increasing $Re_{\tau^\star}$.

The ratio $h'_{t_{rms}}/h'_{rms}$ is a structure parameter of the turbulent flow that can be expressed in terms of correlation coefficients by (4.7). Squaring (4.7*a*) relating the streamwise fluxes (4.5*a*) yields

$$(4.7a) \implies 2c_{h'u'}\, h'_{rms}\, \bar{u}\, u'_{rms} + \overline{u'^2}\, \bar{u}^2 \approxeq c^2_{h'_t u'}\, \overline{h'^2_t} - c^2_{h'u'}\, \overline{h'^2}, \tag{4.12}$$

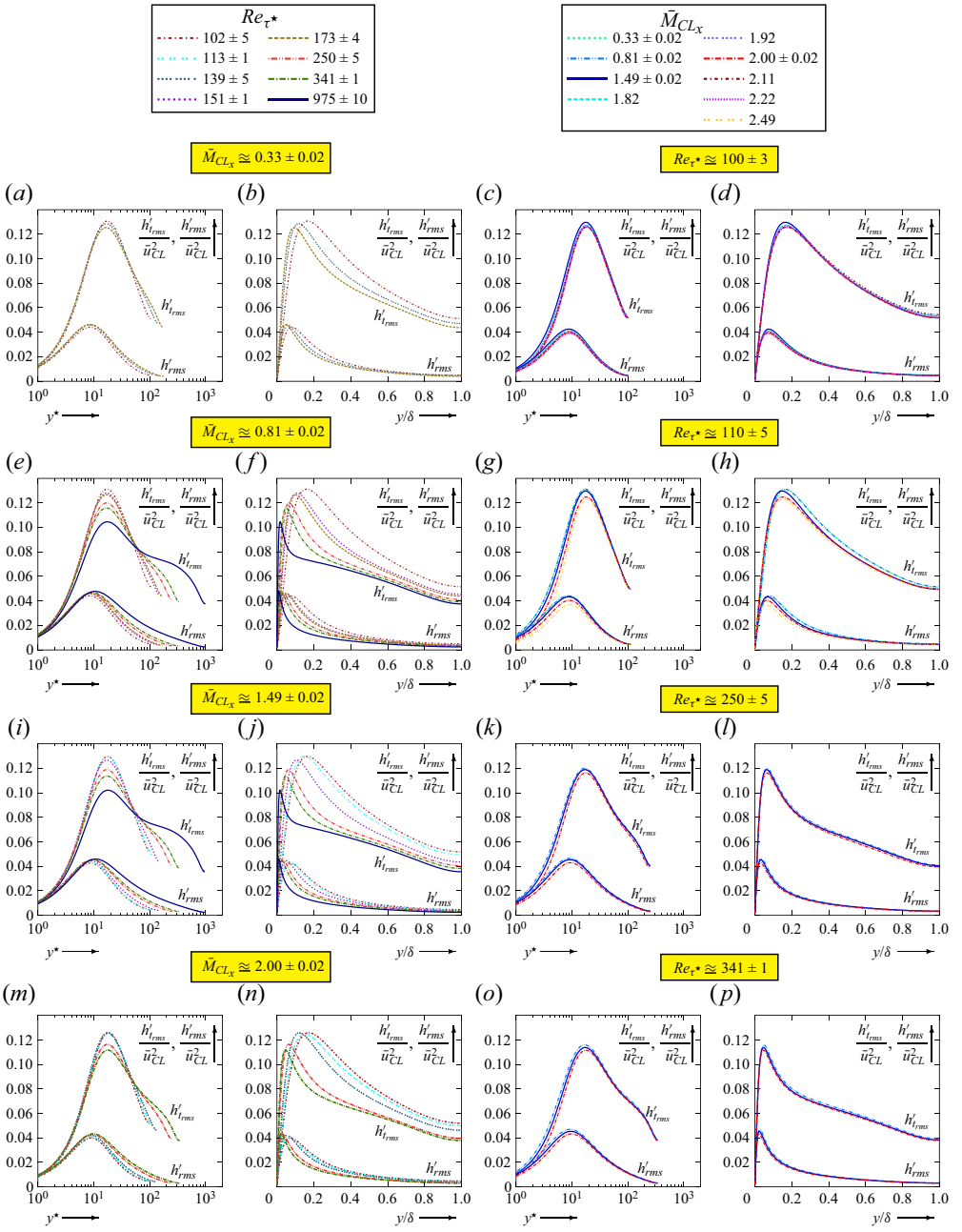

Figure 7. Root mean square fluctuation intensities of total $h'_{t_{rms}}$ and static h'_{rms} enthalpy, scaled by $\bar{u}^2_{CL}$, plotted against inner-scaled ($y^\star$, log scale) and outer-scaled (y/δ, linear) wall distance, for varying HCB Reynolds numbers $97 \leq Re_{\tau^\star} \leq 985$ at nearly constant centreline Mach numbers $\bar{M}_{CL_x} \in \{0.33, 0.80, 1.50, 2.00\}$, and for varying $0.32 \leq \bar{M}_{CL_x} \leq 2.49$ at nearly constant $Re_{\tau^\star} \in \{100, 110, 250, 340\}$, from the present DNS database (table 1).

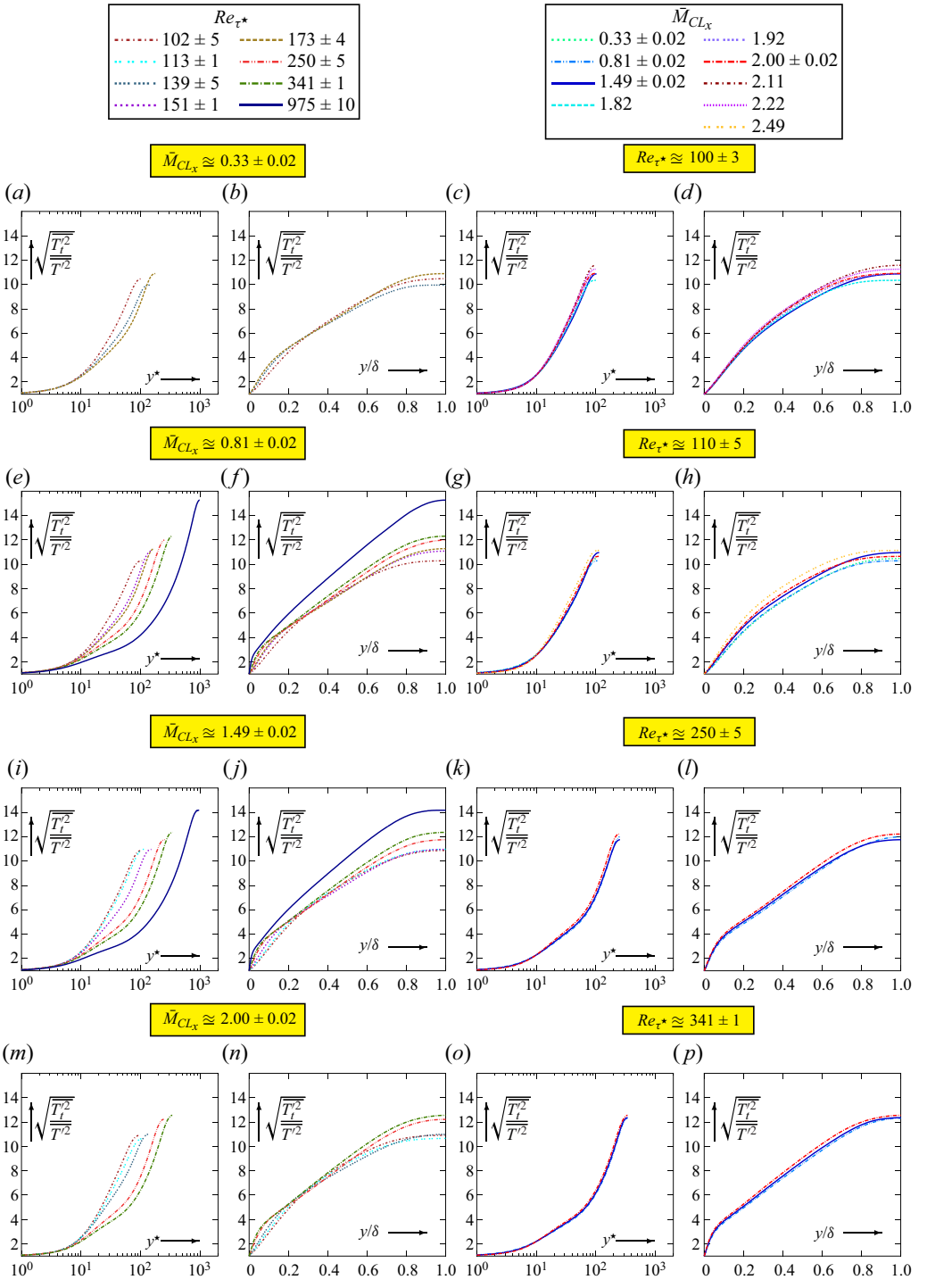

Figure 8. Ratio of total-to-static enthalpy (temperature) fluctuation intensities $h'_{t_{rms}}/h'_{rms} = T'_{t_{rms}}/T'_{rms}$, plotted against inner-scaled ($y^\star$, log scale) and outer-scaled (y/δ, linear) wall distance, for varying HCB Reynolds numbers $97 \leq Re_{\tau^\star} \leq 985$ at nearly constant centreline Mach numbers $\bar{M}_{CL_x} \in \{0.33, 0.80, 1.50, 2.00\}$, and for varying $0.32 \leq \bar{M}_{CL_x} \leq 2.49$ at nearly constant $Re_{\tau^\star} \in \{100, 110, 250, 340\}$, from the present DNS database (table 1).

and replacing (4.7*d*) in (4.12) yields

$$(4.7d),\,(4.7a),\,(4.12)\implies (1-c^2_{h'u'})\overline{h'^2}\approxeq(1-c^2_{h'_tu'})\,\overline{h'^2_t}\implies\frac{h'_{t_{rms}}}{h'_{rms}}\approxeq\sqrt{\frac{1-c^2_{h'u'}}{1-c^2_{h'_tu'}}}. \tag{4.13}$$

The only approximation in (4.13) comes from neglecting HoMs in (4.3) to obtain (4.7). By (4.13), for this particular class of VCW flows (4.1), the observed large values of the $h'_{t_{rms}}/h'_{rms}$ ratio (figure 8) imply that $c^2_{h'_tu'}$ is much closer to 1 than $c^2_{h'u'}$, i.e. that in VCW turbulence, $h_{t'}$ is expected to be correlated very strongly with u'. This is in contrast with adiabatic wall flows (Zhang *et al.* 2014), where h' is correlated very strongly with u', and the ratio $h'_{t_{rms}}/h'_{rms}$ is small. This analysis suggests examining the CCs of static and total enthalpy–transport in order to gain further insight into the turbulence structure of the flow (§ 4.4).

4.4. *Correlation coefficients*

Certainly the most important result observed in the DNS data is that h'_t is very strongly correlated with u' (figure 9), for all $(Re_{\tau^\star},\bar{M}_{CL_x})$ in the database (table 1) everywhere in the channel (for all y). This result is specific to the VCW condition of the TPC flows studied in this work, and does not apply to adiabatic wall turbulence. In the wake region (figures 9*a*,*e*,*i*,*m*), the CC $c_{h'_tu'}$ (4.6) is very close to 1 ($c_{h'_tu'}\approxeq 0.997$), with slightly lower, $Re_{\tau^\star}$-dependent, but still extremely close to 1, values at the wall ($c_{h'_tu'}\gtrapprox 0.98$ for all $Re_{\tau^\star}$). The very strong (h'_t,u') correlation is further confirmed by the close similarity of the profiles of the CCs (4.6) $c_{h'_tv'}$ and $c_{u'v'}$ (figures 9*b*,*f*,*j*,*n*), whose ratio is invariably very close to 1 ($c_{u'v'}/c_{h'_tv'}\sim 1\pm 4\,\%$ for all $y^\star\gtrapprox 5$), except closer to the wall ($y^\star\lessapprox 5$) where slightly higher values are observed (not plotted). Similarly to the outer-scaled fluctuation levels $h'_{t_{rms}}/\bar{u}^2_{CL}$ and $h'_{rms}/\bar{u}^2_{CL}$ (figures 7*c*,*g*,*k*,*o*), $c_{h'_tu'}$ (figures 9*c*,*g*,*k*,*o*) and the ratio $c_{u'v'}/c_{h'_tv'}$ (figures 9*d*,*h*,*l*,*p*) show little sensitivity to $\bar{M}_{CL_x}$, at constant $Re_{\tau^\star}$, except in the near-wall region ($y^\star\lessapprox 10$) for $\bar{M}_{CL_x}\gtrapprox 2$.

The fact that the deviation of the ratio $c_{u'v'}/c_{h'_tv'}$ (figures 9*b*,*f*,*j*,*n*) from unity is larger than that of the CC $c_{h'_tu'}$ (figures 9*a*,*e*,*i*,*m*) highlights the existence of an uncorrelated (with u') part of h'_t, which correlates differently with v'. Experience with the analysis of thermodynamic fluctuations in compressible turbulence (Gerolymos & Vallet 2018) shows that assuming CCs strictly $=\pm 1$ always leads to singular behaviour. The small deviations of $c_{h'_tu'}$ and $c_{u'v'}/c_{h'_tv'}$ from unity are essential in (4.13) and other truncated-to-2oMs relations (4.7), (4.11*b*), as these would be reduced to SRA relations by setting these coefficients equal to exactly 1 (§ 5.2).

In contrast to h'_t (figure 9), h' is not correlated in any particular way to u' (figure 10), $c_{h'u'}$ decreasing from $\sim$1 at the wall to small values ($\sim$0.2) at the centreline, while the ratio $c_{u'v'}/c_{h'v'}=c_{u'v'}/c_{T'v'}$ increases significantly from $\sim$1 near the wall to $\sim$1.45 at the centreline. Both $c_{h'u'}$ and the ratio $c_{u'v'}/c_{h'v'}$ vary with $(Re_{\tau^\star},\bar{M}_{CL_x})$. Therefore, weak Reynolds analogies specific to the class of flows studied in the paper (see (4.1)) could be constructed based on h'_t correlations, rather than on direct instantaneous h' analogies as in the SRA (Huang *et al.* 1995).

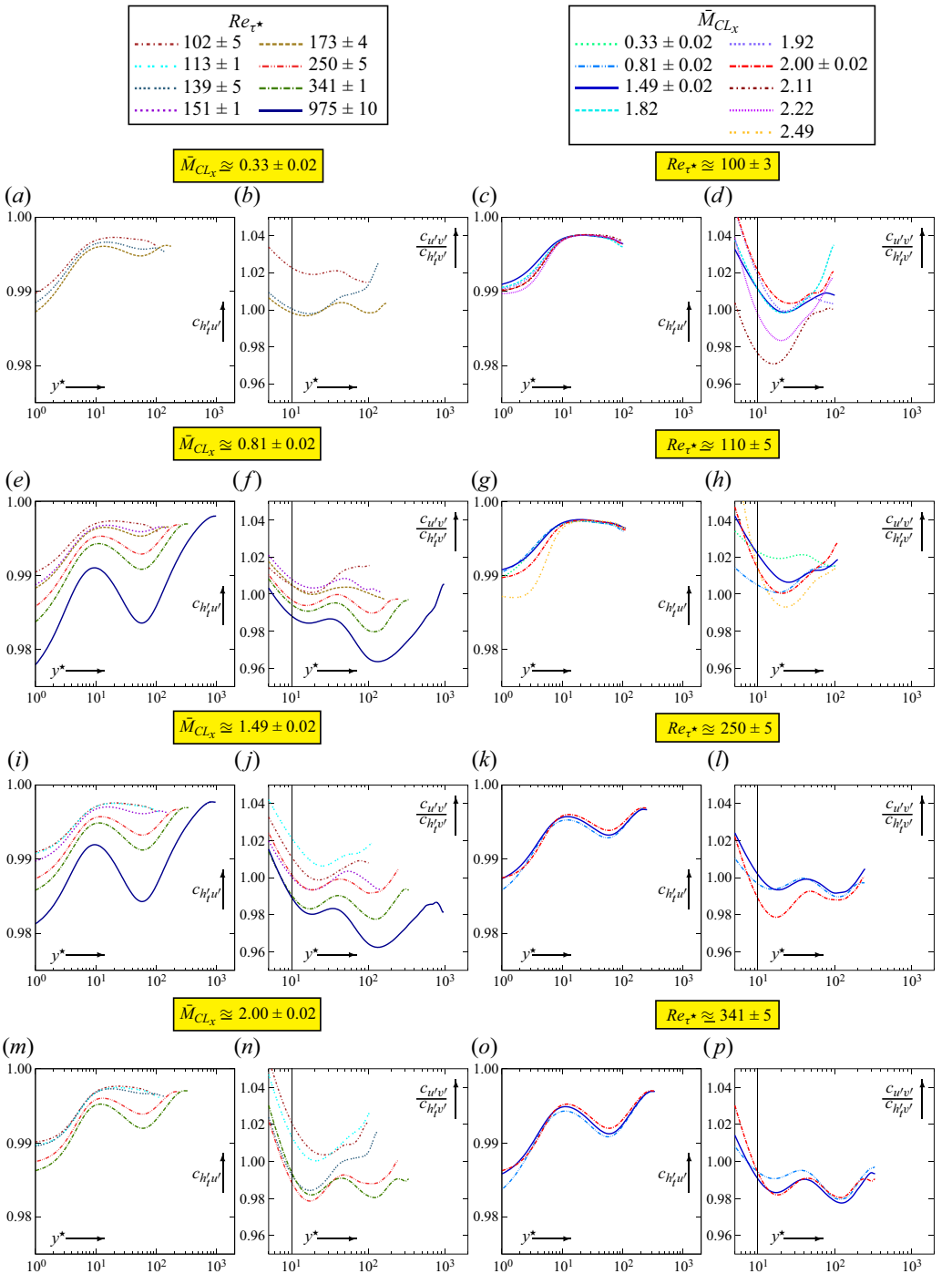

Figure 9. The CC $c_{h'_t u'}$ of streamwise h'_t transport and ratio of CCs $c_{u'v'}/c_{h'_t v'}$ of wall-normal transport of momentum and total enthalpy, plotted against inner-scaled ($y^\star$, log scale) wall distance, for varying HCB Reynolds numbers $97 \leq Re_{\tau^\star} \leq 985$ at nearly constant centreline Mach numbers $\bar{M}_{CL_x} \in \{0.33, 0.80, 1.50, 2.00\}$, and for varying $0.32 \leq \bar{M}_{CL_x} \leq 2.49$ at nearly constant $Re_{\tau^\star} \in \{100, 110, 250, 340\}$, from the present DNS database (table 1).

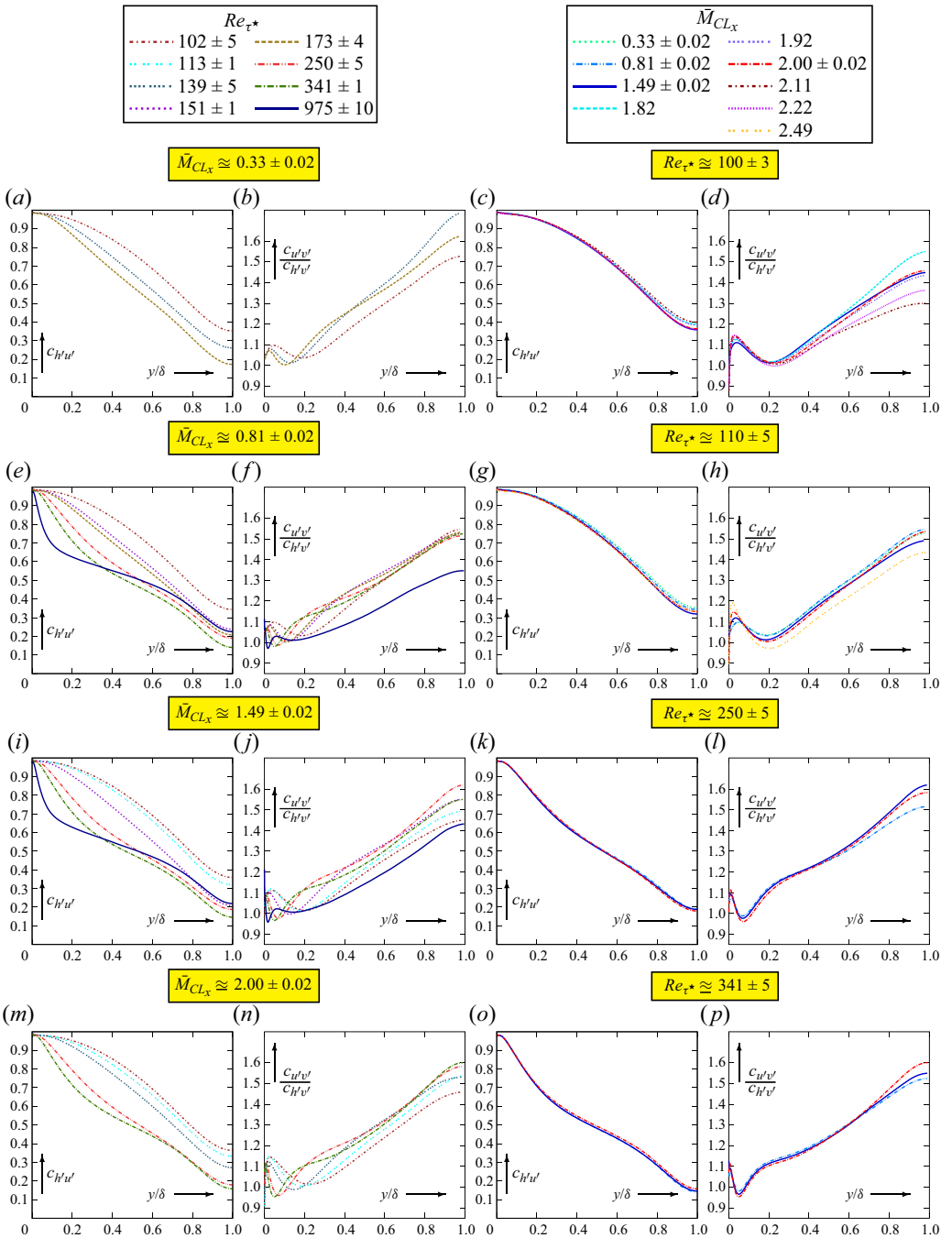

Figure 10. The CC $c_{h'u'}$ of streamwise h' transport and ratio of CCs $c_{u'v'}/c_{h'v'}$ of wall-normal transport of momentum and static enthalpy, plotted against outer-scaled (y/δ, linear) wall distance, for varying HCB Reynolds numbers $97 \leq Re_{\tau^\star} \leq 985$ at centreline Mach numbers $\bar{M}_{CL_x} \in \{0.33, 0.80, 1.50, 2.00\}$, and for varying $0.32 \leq \bar{M}_{CL_x} \leq 2.49$ at nearly constant $Re_{\tau^\star} \in \{100, 110, 250, 340\}$, from the present DNS database (table 1).

4.5. *Joint p.d.f.s*

Further insight into the very strong correlation between h'_t and u' (figure 9) is gained by examining the joint p.d.f. $f_{h'_t u'}$ and comparing it with the joint p.d.f. $f_{h'u'}$ between h' and u' (figure 11), whose correlation diminishes significantly moving away from the wall (figure 10). Those p.d.f. bins for which no hits were recorded were left blank, highlighting the extreme events boundaries.

The CCs can be calculated by integration of these joint p.d.f.s:

$$c_{h'_t u'} \overset{(4.2a)}{=} \int_{h'_{t_{min}}}^{h'_{t_{max}}} \int_{u'_{min}}^{u'_{max}} h'_t u' f_{h'_t u'}(h'_t, u') \,\mathrm{d}\left(\frac{h'_t}{h'_{t_{rms}}}\right) \mathrm{d}\left(\frac{u'}{u'_{rms}}\right), \tag{4.14a}$$

$$c_{h'u'} \overset{(4.2a)}{=} \int_{h'_{min}}^{h'_{max}} \int_{u'_{min}}^{u'_{max}} h' u' f_{h'u'}(h', u') \,\mathrm{d}\left(\frac{h'}{h'_{rms}}\right) \mathrm{d}\left(\frac{u'}{u'_{rms}}\right). \tag{4.14b}$$

The joint p.d.f. $f_{h'_t u'}$ (figures 11*a*,*e*,*i*,*m*,*q*) shows that all (u', h'_t) events are very tightly clustered along the diagonal of the positive ($u'h'_t > 0$) quadrants, a level of very small probability $f_{h'_t u'} = 10^{-4}$ being reached at distances ($|u'| < \frac{1}{2}u'_{rms}$, $|h'_t| < \frac{1}{2}h'_{t_{rms}}$) from the diagonal (figures 11*a*,*e*,*i*,*m*,*q*). Furthermore, except very near the wall ($y^\star < 15$, figure 11*a*), no events are observed at distances greater than $(u'_{rms}, h'_{t_{rms}})$ from the diagonal, these distances shrinking when moving away from the wall (figures 11*e*,*i*,*m*,*q*). Since events in the negative ($u'h'_t < 0$) quadrants occur only very close to the centre $(u', h'_t) = (0, 0)$, the integrand $h'_t u' f_{h'_t u'}(h'_t, u')$ for the evaluation of $c_{h'_t u'}$ in (4.14*a*) shows two positive peaks elongated along the diagonal, one in each of the positive ($u'h'_t > 0$) quadrants (figures 11*c*,*g*,*k*,*o*,*s*). Notice that very near the wall ($y^\star \cong 1$, figure 11*c*), rare events appear much further above the diagonal, albeit with very low probability of occurrence (figure 11*a*). In the near-wall and buffer regions (figures 11*a*,*e*), off-diagonal (u', h'_t) events have slightly higher probability $f_{h'_t u'}$ than further away from the wall (figures 11*m*,*q*), leading to the observed (figure 9) slightly higher deviation of $c_{h'_t u'}$ from unity.

Very near the wall ($y^\star \cong 1$, figure 11), where $(u^2)' \ll h' \Rightarrow h'_t \cong h'$ by (4.3*e*), the joint p.d.f.s $f_{h'_t u'}$ and $f_{h'u'}$ are very similar (figures 11*a*,*b*). However, moving away from the wall, $f_{h'u'}$ spreads away from the diagonal, the more so with increasing distance from the wall (figures 11*f*,*j*,*n*,*r*). As a result, events in the negative ($u'h' < 0$) quadrants occur with increasing probability (figures 11*d*,*h*,*l*,*p*,*t*), contributing negatively to the integrand $h'u' f_{h'u'}(h', u')$ for the evaluation of $c_{h'u'}$ in (4.14*b*), and causing the progressive decorrelation between h' and u' (figure 10) with increasing distance from the wall.

It should be noted that this very strong (u', h'_t) correlation is specific to the class of VCW flows studied. Scatter plots in TBL studies with adiabatic and progressively colder walls (Hadjadj *et al.* 2015, figure 21, p. 435) show clearly that as the wall gets hotter towards adiabatic, the (u', h'_t) events scatter progressively further and further away from the diagonal, reducing the CC.

5. Successes and limitations of the SRA

Weak Reynolds analogy forms use CCs to obtain quite accurate relations between turbulent moments (4.7), (4.13). Ultimately, both $h'_{t_{rms}}$ and h'_{rms} are proportional to u'_{rms} (4.11),

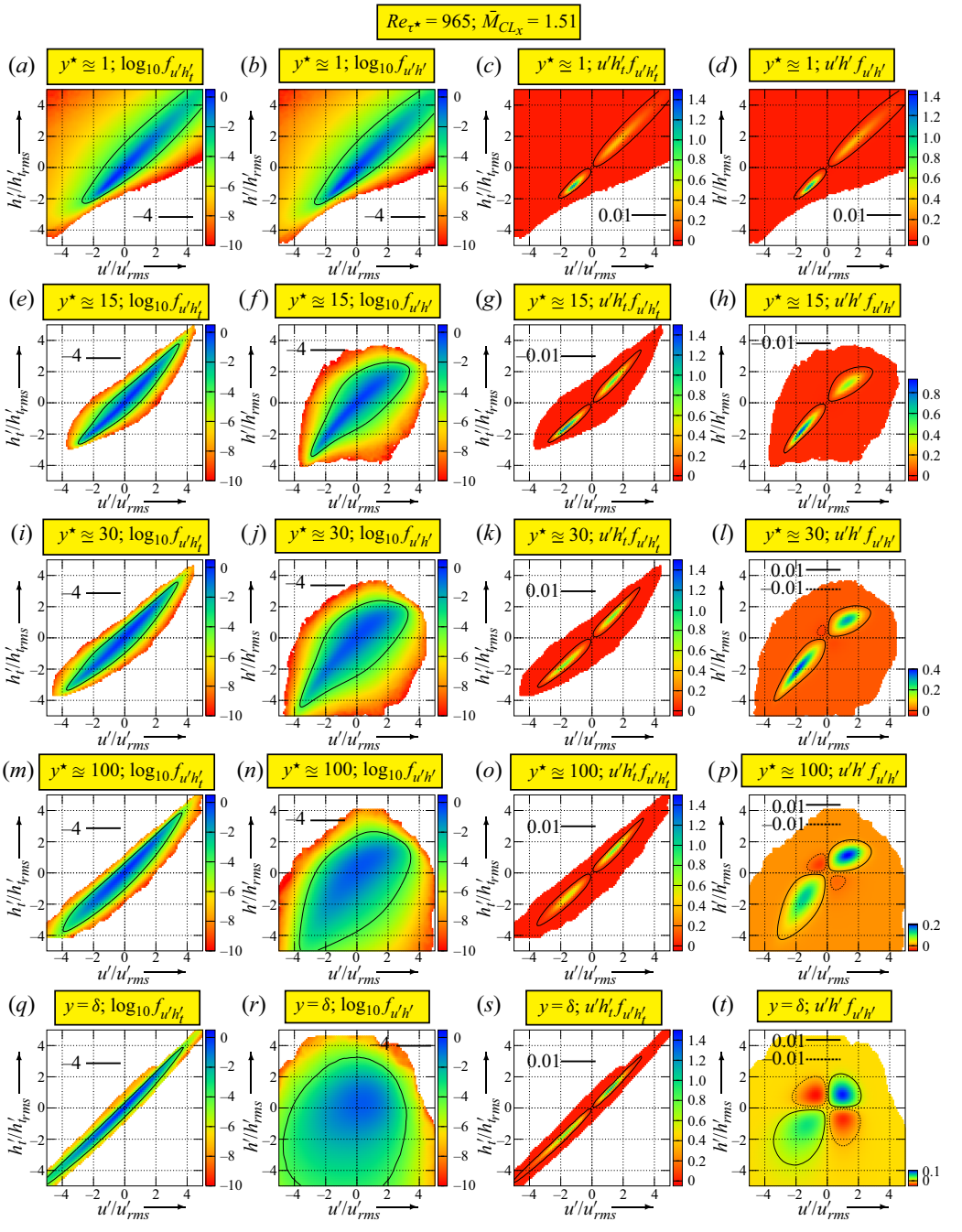

Figure 11. Joint p.d.f.s ($\log_{10}$) of streamwise velocity u' and enthalpy (total h'_t and static h') fluctuations and integrands for the calculation of the CCs $c_{h'_t u'}$ (4.14*a*) and $c_{h' u'}$ (4.14*b*), plotted against the standardised variables (u'/u'_{rms}, $h'_t/h'_{t_{rms}}$, h'/h'_{rms}), at different inner-scaled wall distances $y^\star \in \{1, 15, 30, 100, \delta^\star\}$, at $(Re_{\tau^\star}, \bar{M}_{CL_x}) = (965, 1.51)$, from the present DNS database (table 1).

but with proportionality coefficients that are functions of CCs of velocity and enthalpy transport. The SRAs postulate instead some direct instantaneous proportionality between h' and u' (§ 5.1). Although the SRA is generally successful in predicting h'_{rms}, it may be less successful in predicting $h'_{t_{rms}}$ for less-cold-wall flows, or the ratio $h'_{t_{rms}}/h'_{rms}$, especially in the outer part of the flow. This drawback can be traced to the inherent error in the prediction of CCs by the SRA that can be corrected only by using weak Reynolds analogy approaches (§ 5.2).

5.1. *HCB-SRA*

The SRA proposed by Huang *et al.* (1995, (4.8)–(4.10), p. 208) reads

$$\left.\frac{T'\,\bar{u}}{\bar{T}\,(\gamma-1)\,\bar{M}^2\,u'}\right|_{SRA} \approxeq \frac{1}{Pr_{h'}}\,\frac{\dfrac{\mathrm{d}\bar{T}}{\mathrm{d}y}}{\dfrac{\mathrm{d}\bar{T}_t}{\mathrm{d}y}-\dfrac{\mathrm{d}\bar{T}}{\mathrm{d}y}} \overset{(2.1),\,(4.4)}{\Longrightarrow} h'|_{SRA} \approxeq \frac{1}{Pr_{h'}}\,\frac{\mathrm{d}\bar{h}}{\mathrm{d}\bar{u}}\,u', \tag{5.1}$$

which is essentially the relation given in Huang *et al.* (1995, (4.9), p. 208). It is straightforward, from this basic instantaneous HCB-SRA (5.1), to calculate variances and correlations

$$\text{DNS data:}\quad \{\bar{u},\,u'_{rms},\,\overline{u'v'},\,\bar{h}(\bar{u}),\,Pr_{h'}\}, \tag{5.2a}$$

$$h'|_{SRA}=\frac{1}{Pr_{h'}}\,\frac{\mathrm{d}\bar{h}}{\mathrm{d}\bar{u}}\,u' \Longrightarrow \begin{cases} h'_{rms}|_{SRA}=\left|\dfrac{1}{Pr_{h'}}\,\dfrac{\mathrm{d}\bar{h}}{\mathrm{d}\bar{u}}\right|u'_{rms}, \\ h'_{t_{rms}}|_{SRA}=\left|\left(\dfrac{1}{Pr_{h'}}\,\dfrac{\mathrm{d}\bar{h}}{\mathrm{d}\bar{u}}+\bar{u}\right)\right|u'_{rms}, \\ \overline{h'u'}|_{SRA}=h'_{rms}|_{SRA}\,u'_{rms} & \Longrightarrow\ |c_{h'u'}|_{SRA}=1, \\ \overline{h'_t u'}|_{SRA}=h'_{t_{rms}}|_{SRA}\,u'_{rms} & \Longrightarrow\ \left|c_{h'_t u'}\right|_{SRA}=1, \\ \overline{h'v'}|_{SRA}=\dfrac{1}{Pr_{h'}}\,\dfrac{\mathrm{d}\bar{h}}{\mathrm{d}\bar{u}}\,\overline{u'v'} & \Longrightarrow\ |c_{h'v'}|_{SRA}=|c_{u'v'}|, \\ \overline{h'_t v'}|_{SRA}=\left(\dfrac{1}{Pr_{h'}}\,\dfrac{\mathrm{d}\bar{h}}{\mathrm{d}\bar{u}}+\bar{u}\right)\overline{u'v'} & \Longrightarrow\ \left|c_{h'_t v'}\right|_{SRA}=|c_{u'v'}|, \end{cases} \tag{5.2b}$$

where the truncated expression (4.3*b*) $\Rightarrow h'_t \approxeq h'+\bar{u}\,u'$ was used.

This HCB-SRA (Huang *et al.* 1995) was developed precisely using data for the class of VCW flows studied in the paper, and relations (5.2*b*) perform reasonably well, for each individual moment (figure 12). Probably the most inaccurate prediction is that of the streamwise flux $\overline{h'u'}$. At low $Re_{\tau^\star} \lessapprox 180$ (figures 12*c*,*d*,*o*,*p*), the SRA prediction of $\overline{h'u'}$ is reasonably accurate, both at nearly incompressible $\bar{M}_{CL_x}=0.35$ (figures 12*c*,*d*) and at high supersonic $\bar{M}_{CL_x}=2.49$ (figures 12*o*,*p*). However, at higher $Re_{\tau^\star}=342$ (figures 12*k*,*l*), the agreement of SRA with DNS deteriorates, regarding both the near-wall peak (figure 12*k*) and the outer part of the flow (figure 12*l*), and is even worse at higher $Re_{\tau^\star}=965$ (figures 12*g*,*h*). Recalling that by construction, SRA has the structural deficiency $|c_{h'u'}|_{SRA}=1$, these discrepancies can be explained by the actual behaviour of $c_{h'u'}$ in this VCW flow, which is practically $\bar{M}_{CL_x}$-independent at constant $Re_{\tau^\star}$

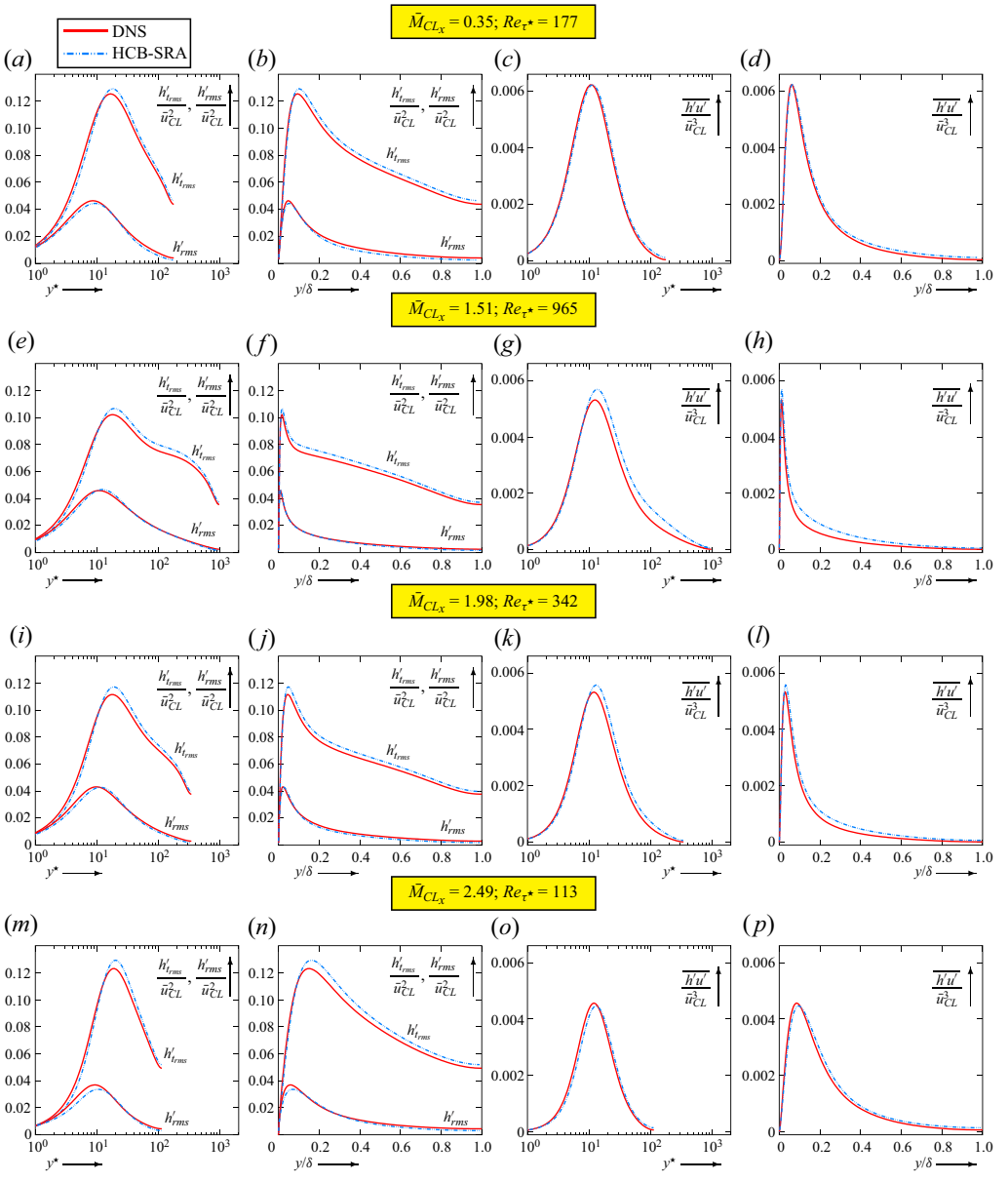

Figure 12. Comparison of DNS data with the predictions HCB–SRA (5.2), for $h'_{t_{rms}}$, h'_{rms}, $\overline{h'u'}$, plotted against inner-scaled ($y^\star$, log scale) and outer-scaled (y/δ, linear) wall distance, for selected flows in the database (table 1), covering the ranges $113 \leq Re_{\tau^\star} \leq 965$ and $0.35 \leq \bar{M}_{CL_x} \leq 2.49$.

(figures 10*c*,*g*,*k*,*o*). With increasing $Re_{\tau^\star}$ (figures 10*a*,*e*,*i*,*m*), $c_{h'u'}$ takes progressively lower values in the outer part of the flow, and although the centreline value seems to stabilise around 0.2 (figures 10*e*,*i*), the outer region penetrates closer to the wall with increasing $Re_{\tau^\star}$, thus spreading the discrepancy in the SRA prediction to a larger part of the flow (figures 12*g*,*h*,*k*,*l*).

Regarding fluctuation intensities $h'_{t_{rms}}$ and h'_{rms}, the accuracy of the SRA does not depend in any particular way on either $Re_{\tau^\star}$ or $\bar{M}_{CL_x}$, both near the wall (figures 12*a*,*e*,*i*,*m*) and in the outer part of the flow (figures 12*b*,*f*,*j*,*n*). Generally, for $y \gtrapprox 0.1\delta$, $h'_{t_{rms}}$ is slightly overpredicted and h'_{rms} is slightly underpredicted by the SRA (figures 12*b*,*f*,*j*,*n*).

5.2. *Limitations of the SRA*

Although the discrepancies in the individual predictions of $h'_{t_{rms}}$ and h'_{rms} seem small (figure 12), their cumulative effect induces substantial error in the prediction of the ratio $h'_{t_{rms}}/h'_{rms}$, which is evaluated readily from (5.2*b*) as

$$\left.\frac{h'_{t_{rms}}}{h'_{rms}}\right|_{SRA} = \frac{\dfrac{1}{Pr_{h'}}\dfrac{\mathrm{d}\bar{h}}{\mathrm{d}\bar{u}} + \bar{u}}{\dfrac{1}{Pr_{h'}}\dfrac{\mathrm{d}\bar{h}}{\mathrm{d}\bar{u}}} = 1 + \left[\frac{1}{Pr_{h'}}\frac{1}{\bar{u}}\frac{\mathrm{d}\bar{h}}{\mathrm{d}\bar{u}}\right]^{-1}, \tag{5.3}$$

i.e. increases linearly with the inverse of the non-dimensional quantity (related to the $\bar{h}(\bar{u})$ relation)

$$\frac{1}{Pr_{h'}}\frac{1}{\bar{u}}\frac{\mathrm{d}\bar{h}}{\mathrm{d}\bar{u}} = \frac{1}{Pr_{h'}}\frac{1}{\bar{u}}\frac{\dfrac{\mathrm{d}\bar{h}}{\mathrm{d}y}}{\dfrac{\mathrm{d}\bar{u}}{\mathrm{d}y}} \overset{(2.1)}{=} \frac{1}{Pr_{h'}}\frac{1}{\bar{u}}\frac{\bar{c}_p\dfrac{\mathrm{d}\bar{T}}{\mathrm{d}y}}{\dfrac{\mathrm{d}\bar{u}}{\mathrm{d}y}} = \frac{1}{Pr_{h'}}\frac{\bar{\mu}\bar{c}_p}{\bar{\lambda}}\frac{\bar{\lambda}\dfrac{\mathrm{d}\bar{T}}{\mathrm{d}y}}{\bar{u}\bar{\mu}\dfrac{\mathrm{d}\bar{u}}{\mathrm{d}y}} \approxeq \frac{\overline{Pr}}{Pr_{h'}}\frac{-\bar{q}_y}{\bar{u}\bar{\tau}_{xy}}, \tag{5.4}$$

where $Pr := \mu c_p/\lambda$ is the molecular Prandtl number, q_y is the wall-normal component of the molecular heat flux, and τ_{xy} is the molecular shear stress. The approximation in (5.4) comes from neglecting the fluctuation of the molecular transport coefficients in $\bar{q}_y = -\overline{\lambda d_y T} = -\bar{\lambda} d_y \bar{T} - \overline{\lambda' d_y T'}$, $\bar{\tau}_{xy} = \overline{\mu d_y u} = \bar{\mu} d_y \bar{u} + \overline{\mu' d_y u'}$ and $\overline{Pr} \approxeq \bar{\mu}\bar{c}_p/\bar{\lambda}$.

Notice that for the flows studied (table 1), $1/[d_{\bar{u}}\bar{h}/(\bar{u}/Pr_{h'})]$ is 0 at the wall, reaching high Re-dependent values at the centreline region (figure 13*a*). The HCB-SRA predicts (see (5.3)) that $h'_{t_{rms}}/h'_{rms}$ increases linearly with the non-dimensional parameter $1/[d_{\bar{u}}\bar{h}/(\bar{u}/Pr_{h'})]$ in (5.4), in contrast with DNS data, which show a bounded increase (figure 13*b*). This is a general structural deficiency of SRA approaches. Notice first that (4.13) provides no information because SRA assumptions lead to $|c_{h'_t u'}| = |c_{h' u'}| = 1$ in (5.2*b*). The origin of the problem can be traced by using the truncated-to-2oMs relations (4.7) to express the ratio $h'_{t_{rms}}/h'_{rms}$ as a function of the non-dimensional parameter $[d_{\bar{u}}\bar{h}/(\bar{u}/Pr_{h'})]$ and appropriate CCs. As for the class of the VCW flows considered, $c_{h'_t u'}$ and $c_{u'v'}/c_{h'_t v'}$ show little variation (figure 9), except that in the immediate vicinity of the wall, it is practical to use relations involving these CCs. Combining (4.7*c*) and (4.11) leads, after simple calculations, to the generally valid truncated-to-2oMs relation

$$\frac{h'_{t_{rms}}}{h'_{rms}} \overset{(4.7c),\,(4.11)}{\approxeq} \frac{1}{\sqrt{1 + \dfrac{1}{\left[\dfrac{c_{u'v'}}{c_{h'_t v'}}\left(\dfrac{1}{Pr_{h'}}\dfrac{1}{\bar{u}}\dfrac{\mathrm{d}\bar{h}}{\mathrm{d}\bar{u}} + 1\right)\right]^2} - \dfrac{2c_{h'_t u'}}{\left|\dfrac{c_{u'v'}}{c_{h'_t v'}}\left(\dfrac{1}{Pr_{h'}}\dfrac{1}{\bar{u}}\dfrac{\mathrm{d}\bar{h}}{\mathrm{d}\bar{u}} + 1\right)\right|}}}, \tag{5.5}$$

showing that the dependence of the ratio $h'_{t_{rms}}/h'_{rms}$ on the non-dimensional parameter $[d_{\bar{u}}\bar{h}/(\bar{u}/Pr_{h'})]$ is much more complex than the SRA predicts, and depends on the CCs

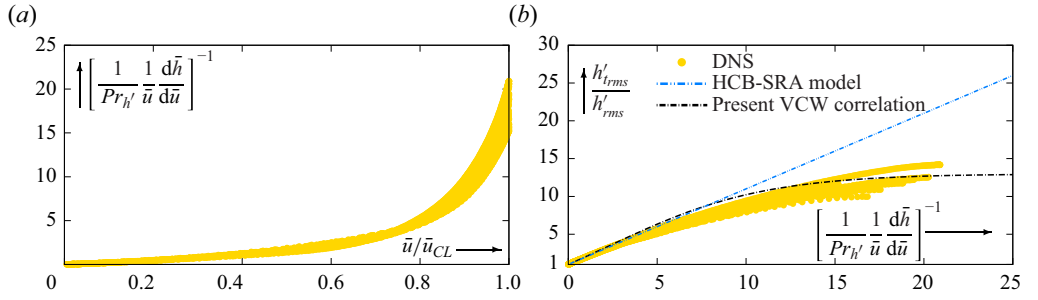

Figure 13. Comparison (b) of DNS data with the predictions of the ratio $h'_{t_{rms}}/h'_{rms}$ by HCB-SRA (5.3) and by the VCW correlation (5.6) as a function of the non-dimensional parameter $1/[d_{\bar{u}}\tilde{h}/(\bar{u}/Pr_{h'})]$ (5.4), and DNS profiles (a) of this parameter against $\bar{u}/\bar{u}_{CL}$; all available DNS data (table 1) in the ranges $97 \leq Re_{\tau^\star} \leq 985$ and $0.32 \leq \bar{M}_{CL_x} \leq 2.49$ are plotted.

$\{c_{h'_t u'}, c_{u'v'}/c_{h'_t v'}\}$. The fundamental structural default of the SRA is that it invariably predicts $|c_{h'u'}|_{SRA} = |c_{h'_t u'}|_{SRA} = |c_{u'v'}/c_{h'v'}|_{SRA} = 1$ (see (5.2b)) because of the postulated instantaneous strict proportionality $h' \propto u$ for all t. Notice that using these SRA values in (5.5) reverts readily to (5.3).

For the particular VCW class of flows studied in the paper, DNS data suggest average values $(c_{h'_t u'})_{VCW} \approxeq 0.997$ (figures 9a,e,i,m) and $(c_{u'v'}/c_{h'_t v'})_{VCW} \approxeq 0.97$ (figures 9b,f,j,n), leading to the specific correlation for these VCW flows

$$\left.\frac{h'_{t_{rms}}}{h'_{rms}}\right|_{VCW} \approxeq \frac{1}{\sqrt{1+\dfrac{1}{\left[0.97\left(\dfrac{1}{Pr_{h'}}\dfrac{1}{\bar{u}}\dfrac{\mathrm{d}\bar{h}}{\mathrm{d}\bar{u}}+1\right)\right]^2}-\dfrac{2\times 0.997}{\left|0.97\left(\dfrac{1}{Pr_{h'}}\dfrac{1}{\bar{u}}\dfrac{\mathrm{d}\bar{h}}{\mathrm{d}\bar{u}}+1\right)\right|}}}, \tag{5.6}$$

which corrects quite satisfactorily the SRA prediction, giving close agreement with DNS data (figure 13b). Of course, correlation (5.6) is limited to the present class of flows (table 1) and is not applicable to flows with different enthalpy rise (equivalently wall heat flux) conditions, for which the general relation (5.5) applies. Finally, it is significant to notice how strong is the effect of the very small departures of $(c_{h'_t u'})_{VCW}$, $(c_{u'v'}/c_{h'_t v'})_{VCW}$ from unity in (5.6).

6. Transport equations of fluctuating enthalpy variance and fluxes

In addition to the structural difficulties of the SRA (§ 5.2), the DNS results revealed a complex dependence of Pr_T (4.8), in the near-wall $y^\star \lessapprox 10$ region, with respect to both $Re_{\tau^\star}$ (figures 5a,e,i,m) and $\bar{M}_{CL_x}$ (figures 5c,g,k,o). We examine the transport equations for $\overline{\rho h''^2}$ and $\overline{\rho h'' u''_i}$ to gain insight into the mechanisms behind this near-wall behaviour.

Under equation of state (2.1), the equations for static enthalpy or temperature are the same to a factor c_p (Gerolymos & Vallet 2014, (2.4e), (2.4f), p. 709). The transport

equation for the fluctuating enthalpy variance reads (Gerolymos & Vallet 2014)

$$\underbrace{\frac{\partial\overline{\rho h''^2}}{\partial t}+\frac{\partial\overline{\rho h''^2}\,\tilde{u}_\ell}{\partial x_\ell}}_{C_{(\rho h''^2)}\overset{(TPC)}{=}0}=\underbrace{-\frac{\partial}{\partial x_\ell}\left(\overline{\rho h''^2u''_\ell}+2\,\overline{h'q'_\ell}\right)}_{d_{(\rho h''^2)}}\underbrace{-2\,\overline{\rho u''_\ell h''}\,\frac{\partial\tilde{h}}{\partial x_\ell}+2\left(\overline{h'\tau'_{m\ell}}\,\bar{S}_{m\ell}+\overline{h'S'_{m\ell}}\,\bar{\tau}_{m\ell}\right)}_{P_{(\rho h''^2)}}$$
$$\underbrace{-\left(-2\,\overline{q'_\ell\,\frac{\partial h'}{\partial x_\ell}}\right)}_{\bar{\rho}\varepsilon_{(\rho h''^2)}}+\underbrace{2\,\overline{h''}\left(\overline{\frac{\mathrm{D}p}{\mathrm{D}t}}+\overline{\tau_{m\ell}S_{m\ell}}-\frac{\partial\bar{q}_\ell}{\partial x_\ell}\right)}_{K_{(\rho h''^2)}}+\underbrace{2\,\overline{h'\tau'_{m\ell}S'_{m\ell}}}_{\Xi_{(\rho h''^2)}}+\underbrace{2\,\overline{h'\left(\frac{\mathrm{D}p}{\mathrm{D}t}\right)'}}_{\Upsilon_{(\rho h''^2)}},\tag{6.1a}$$

where $C_{(\rho h''^2)}$ represents convection by the mean flow ($=0$ in TPC flow), $d_{(\rho h''^2)}$ represents turbulent and molecular diffusion, $P_{(\rho h''^2)}$ represents production by mean flow gradients, $\varepsilon_{(\rho h''^2)}>0$ represents destruction by molecular heat conductivity, $K_{(\rho h''^2)}$ are direct compressibility (density fluctuation) effects, $\Xi_{(\rho h''^2)}$ are triple correlations which together with the corresponding terms in $P_{(\rho h''^2)}$ sum up to $2\,\overline{h'\tau_{m\ell}S_{m\ell}}$, and $\Upsilon_{(\rho h''^2)}$ represents coupling with $(\mathrm{D}_t p)'$ which was identified by Le Ribault & Friedrich (1997) as a compressibility effect in line with (3.2). The influence of $K_{(\rho h''^2)}$ or $\Upsilon_{(\rho h''^2)}$ in the budgets of (6.1*a*) is negligibly small (figure 14*a*). Very close to the wall ($y^\star\lessapprox 1$), the budgets of (6.1*a*) are a balance between diffusion $d_{(\rho h''^2)}$ (essentially molecular $-2d_y\,\overline{h'q'_y}$) and destruction $-\rho\varepsilon_{(\rho h''^2)}$ (figure 14*a*). In the outer part of the flow ($y\gtrapprox 0.7\delta$), $P_{(\rho h''^2)}+\Xi_{(\rho h''^2)}$ cancel out so that the remaining budgets are a balance between diffusion $d_{(\rho h''^2)}$ (essentially turbulent $-d_y\,\overline{\rho h''^2v''}$) and destruction $-\rho\varepsilon_{(\rho h''^2)}$ (figure 14*a*). In the near-wall region ($4\lessapprox y^\star\lessapprox 100$), production $P_{(\rho h''^2)}+\Xi_{(\rho h''^2)}$ is important and balances diffusion and destruction $d_{(\rho h''^2)}-\rho\varepsilon_{(\rho h''^2)}$ (figure 14*a*).

The transport equations for the fluxes $\overline{\rho h''u''_i}$,

$$\underbrace{\frac{\partial\overline{\rho h''u''_i}}{\partial t}+\frac{\partial\overline{\rho h''u''_i}\,\tilde{u}_\ell}{\partial x_\ell}}_{C_{(\rho h''u''_i)}}=\underbrace{-\frac{\partial\overline{\rho h''u''_iu''_\ell}}{\partial x_\ell}+\frac{\partial\overline{h'\tau'_{i\ell}}}{\partial x_\ell}-\frac{\partial}{\partial x_\ell}\left(\overline{u'_iq'_\ell}\right)}_{d_{(\rho h''u''_i)}}$$

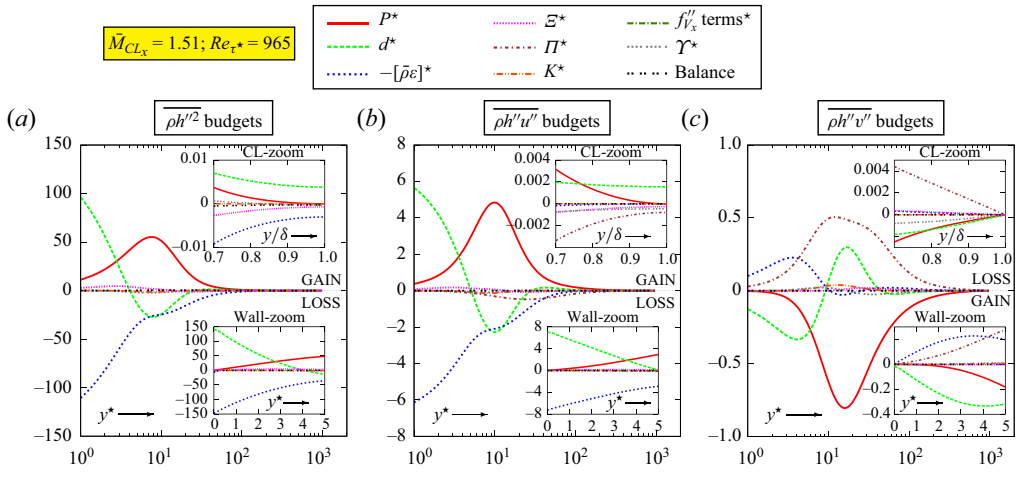

Figure 14. Budgets, at $(Re_{\tau^\star}, \bar{M}_{CL_x}) = (965, 1.51)$, of the transport equations (6.1*a*) and (6.1*b*), for (*a*) $\overline{\rho h''^2}$, (*b*) $\overline{\rho h'' u''}$ and (*c*) $\overline{\rho h'' v''}$, in $(\cdot)^\star$ units, plotted against $y^\star$ (log scale), with wall-zoom (against $y^\star$, linear) and centreline-zoom (against y/δ, linear), from the present DNS database (table 1).

$$\underbrace{-\overline{\rho u_\ell'' h''}\,\frac{\partial \tilde{u}_i}{\partial x_\ell} - \overline{\rho u_i'' u_\ell''}\,\frac{\partial \tilde{h}}{\partial x_\ell} + \left(\overline{u_i' \tau_{m\ell}'}\,\bar{S}_{m\ell} + \overline{u_i' S_{m\ell}'}\,\bar{\tau}_{m\ell}\right)}_{P_{(\rho h'' u_i'')}}$$
$$\underbrace{-\left(-\overline{q_\ell'\,\frac{\partial u_i'}{\partial x_\ell}} + \overline{\tau_{i\ell}'\,\frac{\partial h'}{\partial x_\ell}}\right)}_{\bar{\rho}\varepsilon_{(\rho h'' u_i'')}} + \underbrace{\overline{u_i''}\left(\overline{\frac{\mathrm{D}p}{\mathrm{D}t}} + \overline{\tau_{m\ell} S_{m\ell}} - \frac{\partial \bar{q}_\ell}{\partial x_\ell}\right) + \overline{h''}\left(-\frac{\partial \bar{p}}{\partial x_i} + \frac{\partial \bar{\tau}_{i\ell}}{\partial x_\ell}\right)}_{K_{(\rho h'' u_i'')}}$$
$$\underbrace{+\overline{u_i' \tau_{m\ell}' S_{m\ell}'}}_{\Xi_{(\rho h'' u_i'')}} \underbrace{-\overline{h'\,\frac{\partial p'}{\partial x_i}}}_{\Pi_{(\rho h'' u_i'')}} + \overline{\rho h'' f_{V_i}''} + \underbrace{\overline{u_i'\left(\frac{\mathrm{D}p}{\mathrm{D}t}\right)'}}_{\Upsilon_{(\rho h'' u_i'')}}, \tag{6.1b}$$

in addition to the mechanisms identified in the transport of $\overline{\rho h''^2}$ (6.1*a*), contain the pressure-scrambling term $\Pi_{(\rho h'' u_i'')}$ (Le Ribault & Friedrich 1997), and in the case of the streamwise flux, the term $\overline{\rho h'' f''_{V_x}}$, which is negligibly small everywhere in the channel (figure 14*b*). Notice that for TPC flow,

$$P_{(\rho h'' u'')} + \Xi_{(\rho h'' u'')} \overset{(TPC)}{=} -\overline{\rho h'' v''}\,\frac{\mathrm{d}\tilde{u}}{\mathrm{d}y} - \overline{\rho u'' v''}\,\frac{\mathrm{d}\tilde{h}}{\mathrm{d}y} + \overline{u' \tau_{m\ell} S_{m\ell}}, \tag{6.1c}$$

so Pr_T in (4.8) is precisely the ratio of the production of the streamwise flux $\overline{\rho h'' u''}$ from the enthalpy gradient on its production from shear, offering an alternative interpretation of Pr_T, and highlighting the connection between the streamwise $\overline{\rho h'' u''}$ and wall-normal $\overline{\rho h'' v''}$ fluxes.

In the near-wall region ($y^\star \lessapprox 100$), the same remarks apply to the budgets of the streamwise flux $\overline{\rho h'' u''}$ (figure 14*b*) as for those of the variance $\overline{\rho h''^2}$ (figure 14*a*), with

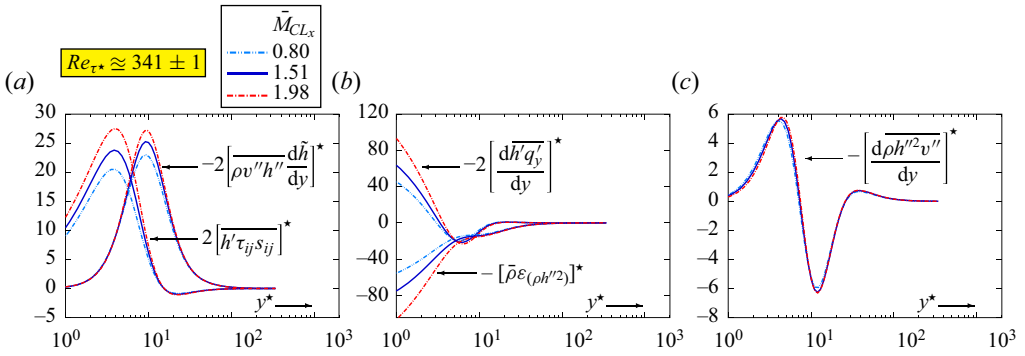

Figure 15. Influence of Mach number $\bar{M}_{CL_x} \in \{0.80, 1.51, 1.98\}$, at nearly constant $Re_{\tau^\star} \approxeq 341 \pm 1$, on various terms in the budgets of the transport equation for the enthalpy variance $\overline{\rho h''^2}$ (6.1*a*), from the present DNS database (table 1), in $(\cdot)^\star$ units, plotted against $y^\star$ (log scale), illustrating both (*a*,*b*) complex non-$(\cdot)^\star$ scaling for some terms, and (*c*) $(\cdot)^\star$ scaling for others.

the significant difference that the pressure-scrambling term $\Pi_{(\rho h'' u'')}$ is comparable to the sum of the others, $d_{(\rho h'' u'')} + P_{(\rho h'' u'')} + \Xi_{(\rho h'' u'')} - \bar{\rho}\varepsilon_{(\rho h'' u'')}$, and therefore has a significant influence on the budgets (figure 14*b*). In the outer part of the flow ($y \gtrapprox 0.7\delta$), destruction of the streamwise flux $-\bar{\rho}\varepsilon_{(\rho h'' u'')}$ is negligibly small, and, as production $P_{(\rho h'' u'')}$ diminishes to 0 approaching the centreline, the budgets are essentially a balance of the positive contribution of turbulent diffusion ($-d_y\,\overline{\rho h'' u'' v''}$) and remaining production $d_{(\rho h'' u'')} + P_{(\rho h'' u'')}$, with the negative contributions of the pressure terms and the triple correlations, $\Xi_{(\rho h'' u'')} + \Pi_{(\rho h'' u'')} + \Upsilon_{(\rho h'' u'')}$ (figure 14*b*), highlighting the importance of the pressure terms almost everywhere ($y^\star \gtrapprox 10$).

The budgets of (6.1*b*) for the wall-normal flux ($VCW \Rightarrow \overline{\rho h'' v''} < 0$ so that negative terms in the budgets count as gain) are completely different, dominated by the positive (loss) pressure-scrambling term $\Pi_{(\rho h'' v'')}$ that opposes the negative (gain) production $P_{(\rho h'' v'')}$, and is the largest term in the outer part of the flow (figure 14*c*). Notice that $\Pi_{(\rho h'' v'')}$ is of the same order of magnitude as its streamwise counterpart $\Pi_{(\rho h'' u'')}$ everywhere, and the orders of magnitude of different mechanisms in the centreline region ($y \gtrapprox 0.7\delta$) are comparable for both components of $\overline{\rho h'' u''_i}$ (figures 14*b*,*c*).

Examination of various terms in the budgets of $\overline{\bar{\rho} h''^2}$ (6.1*a*) at nearly constant $Re_{\tau^\star} \approxeq 341 \pm 1$ shows that only turbulent diffusion $-d_y(\overline{\rho h''^2 v''})$ follows $(\cdot)^\star$ scaling with varying $\bar{M}_{CL_x} \in \{0.80, 1.51, 1.98\}$ (figure 15*c*). Both molecular diffusion $-2[d_y(\overline{h' q'})]^\star$ and destruction $-[\bar{\rho}\varepsilon_{(\rho h''^2)}]^\star$, in $(\cdot)^\star$ units, show substantial near-wall ($y^\star \lessapprox 10$) variation with $\bar{M}_{CL_x}$ (figure 15*b*), and the same applies to the two different mechanisms of the sum

$$P_{(\rho h''^2)} + \Xi_{(\rho h''^2)} \overset{(TPC)}{=} -2\,\overline{\rho h'' v''}\,\frac{\mathrm{d}\tilde{h}}{\mathrm{d}y} + 2\,\overline{h'\tau_{m\ell} S_{m\ell}}, \tag{6.1d}$$

with distinct variation of the peak of $-2[d_y(\overline{\rho h'' v''} d_y \tilde{h})]^\star$ occurring at $y^\star \approxeq 10$ (figure 15*a*) and that of $2[\overline{h'\tau_{m\ell} S_{m\ell}}]^\star$ occurring much closer to the wall, at $y^\star \approxeq 4$ (figure 15*a*). This behaviour contrasts with that of $[\overline{\tau_{m\ell} S_{m\ell}}]^\star$, which does follow $(\cdot)^\star$ scaling near the wall, at constant $Re_{\tau^\star}$ (figure 1*b*).

The strong near-wall $\bar{M}_{CL_x}$ effect on several (figures 15*a*,*b*) but not all (figure 15*c*) of the terms in (6.1*a*) is related to the complex scaling behaviour of the fluxes (figure 16). Recall first that h'_{rms} scales quite well with $\bar{u}^2_{CL}$, both near the wall against $y^\star$ (figures 7*c*,*g*,*k*,*o*), and in the entire channel against y/δ (figures 7*d*,*h*,*l*,*p*). The fluxes $\overline{h'u'_i}$ can scale with the inner $u_{\tau^\star} := \sqrt{(\bar{\tau}_w/\bar{\rho}(y))}$, outer $\bar{u}_{CL}$, or some mixed inner/outer velocity scale. The inner-scaled wall-normal flux $\overline{h'v'}^\star := \overline{h'v'}/u^3_{\tau^\star}$, at constant $Re_{\tau^\star}$, practically collapses on a single curve with varying $\bar{M}_{CL_x}$ (figures 16*d*,*h*,*l*,*p*), showing a general validity of $(\cdot)^\star$ scaling for wall-normal transport, as it obviously also applies to $\overline{\rho h''^2 v''}$ (figure 15*c*), and it is well known that it applies to $\overline{\rho u'' v''}^\star \equiv \overline{\rho u'' v''}^+$ (van Driest 1951; Trettel & Larsson 2016). However, the value of the $\overline{h'v'}^\star$ peak varies very strongly with $Re_{\tau^\star}$ (figures 16*d*,*h*,*l*,*p*), and, although not plotted, continues to increase (in absolute value) for $Re_{\tau^\star} \approxeq 1000$. It appears that outer-scaling the wall-normal flux $\overline{h'v'}/\bar{u}^3_{CL}$ (figures 16*b*,*f*,*j*,*n*) behaves much better with respect to an asymptotic high-Re trend in the near-wall region ($y^\star \lessapprox y^\star_{PEAK_{(h'v')}}$). Notice that, similar to $\overline{\rho u'' v''}^\star \equiv \overline{\rho u'' v''}^+$, $y^\star_{PEAK_{(h'v')}}$ varies strongly with $Re_{\tau^\star}$. On the other hand, the streamwise flux seems to follow mixed scaling $\overline{h'u'}/(\bar{u}^2_{CL}\, u_{\tau^\star})$, regarding both the $\bar{M}_{CL_x}$ effect (figures 16*c*,*g*,*k*,*o*) and the $Re_{\tau^\star}$ effect (figures 16*a*,*e*,*i*,*m*). Considering Favre-averaged fluxes $\overline{\rho h'' u''_i}$ (not shown) yields exactly the same conclusions as those obtained for the Reynolds-averaged fluxes $\overline{h'u'_i}$ (figure 16), in line with the close agreement between Pr_T (4.8) using Favre averages and $Pr_{h'}$ (4.10) using Reynolds averages (figure 6).

7. Conclusions

Thermal turbulence structure of TPC flow depends very little on $\bar{M}_{CL_x}$. Therefore, the centreline-to-wall temperature ratio $\bar{T}_{CL}/\bar{T}_w$, which depends very strongly on $\bar{M}_{CL_x}$, is not appropriate to parametrise the thermal turbulence structure. In contrast the non-dimensional enthalpy rise $(\bar{h}_{CL} - \bar{h}_w)/(\frac{1}{2}\bar{u}^2_{CL})$ is very weakly dependent on $\bar{M}_{CL_x}$ and is probably a much better choice, in line with the relative $\bar{M}_{CL_x}$-independence of the non-dimensional $(\bar{h}(\bar{u}) - \bar{h}_w)/(\frac{1}{2}\bar{u}^2_{CL})$ relation.

The DNS data for the total and static enthalpy variances and correlations, for turbulent plane channel flow in the ranges $100 \lessapprox Re_{\tau^\star} \lessapprox 1000$ and $0.3 \leq \bar{M}_{CL_x} \leq 2.5$, indicate the following.

(i) Joint p.d.f.s of (u', h'_t) show a very strong correlation, with events tightly clustered along the diagonal of the positive quadrants, everywhere in the channel, verified by the correlation coefficient (CC) $c_{h'_t u'}$ and by the ratio of wall-normal transport CCs $c_{u'v'}/c_{h'_t v'}$, both of which are very close to 1.

(ii) In contrast, for the class of very-cold-wall (VCW) flows studied, static enthalpy fluctuations h' are not well correlated with u', the CC $c_{h'u'}$ rapidly decreasing with increasing wall distance, as more and more events in the joint p.d.f.s of (u', h') occur away from the diagonal of the positive quadrants.

(iii) Outside the very-near-wall region ($y^\star \gtrapprox 20$), at nearly constant $Re_{\tau^\star}$, the quantities $h'_{t_{rms}}/\bar{u}^2_{CL}$, $h'_{rms}/\bar{u}^2_{CL}$, $c_{h'_t u'}$, $c_{u'v'}/c_{h'_t v'}$, Pr_T show little sensitivity to $\bar{M}_{CL_x}$, also implying that $\bar{u}^2_{CL}$ is the correct outer scaling for both $h'_{t_{rms}}$ and h'_{rms}.

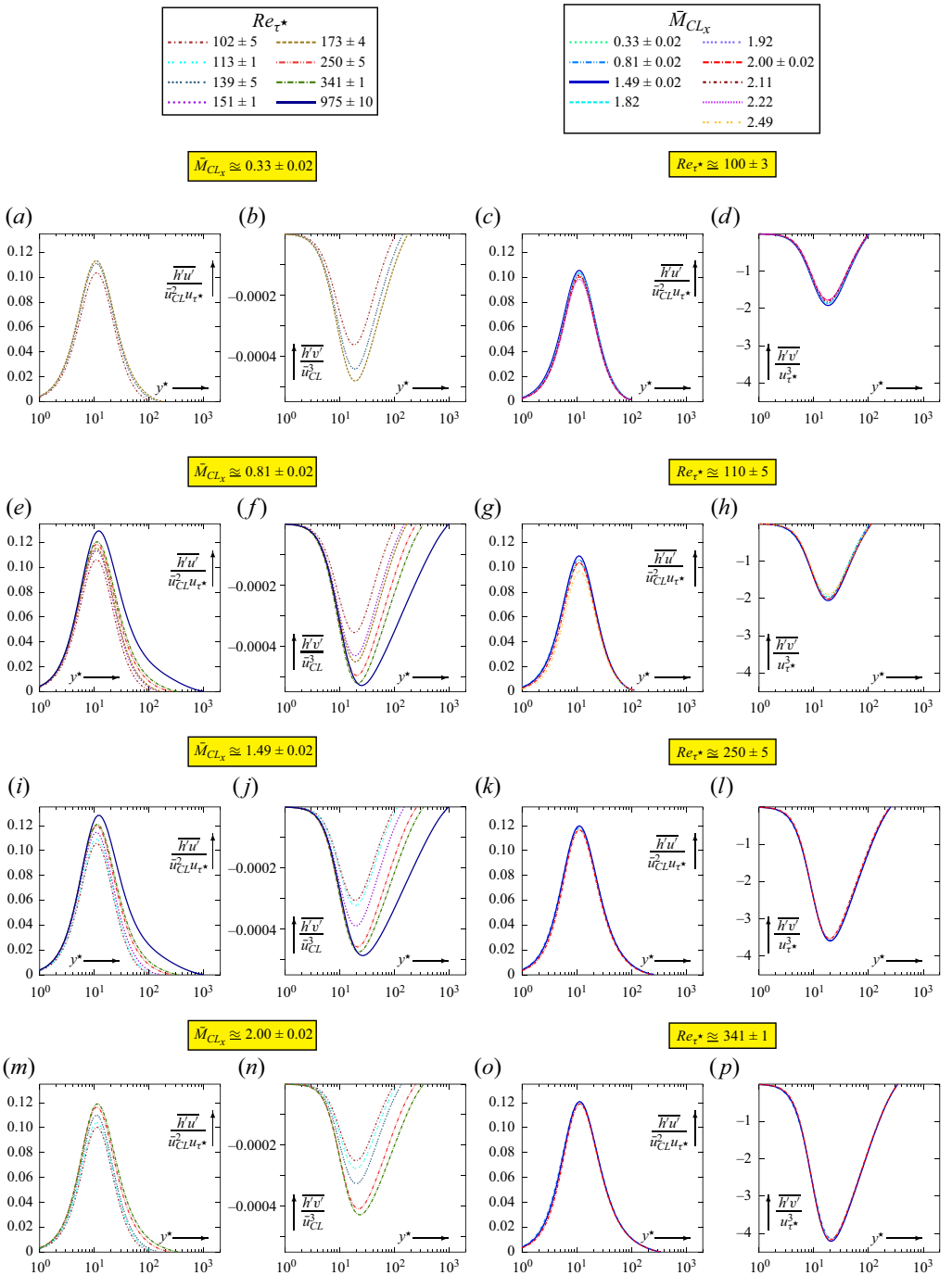

Figure 16. Fluxes $\overline{h'u'}$ (mixed scaled by $\bar{u}^2_{CL}\,u_{\tau\star}$) and $\overline{h'v'}$ (both inner-scaled by $u^3_{\tau\star}$ and outer-scaled by $\bar{u}^3_{CL}$) for turbulent h'-transport, for varying HCB Reynolds numbers $97 \leq Re_{\tau\star} \leq 985$ at centreline Mach numbers $\bar{M}_{CL_x} \in \{0.33, 0.80, 1.50, 2.00\}$, and for varying $0.32 \leq \bar{M}_{CL_x} \leq 2.49$ at nearly constant $Re_{\tau\star} \in \{100, 110, 250, 340\}$, from the present DNS database (table 1).

(iv) At constant $Re_{\tau^\star}$, the inner-scaled wall-normal flux $\overline{h'v'}^\star = \overline{h'v'}/u_{\tau^\star}^3$ is practically independent of $\bar{M}_{CL_x}$ everywhere in the channel, whereas the streamwise flux follows mixed scaling $\overline{h'u'}/(\bar{u}_{CL}^2\, u_{\tau^\star})$.

(v) The higher $Re_{\tau^\star} \approxeq 1000$ data suggest an outer law $(y/\delta)^2$ decay for Pr_T (which also fits lower $Re_{\tau^\star} \gtrapprox 250$ data), highlighting at the same time the need for higher-$Re_{\tau^\star}$ data to elucidate the high-Re asymptotics.

The HCB–SRA predicts reasonably well $h'_{t_{rms}}$, h'_{rms}, $\overline{h'u'}$ for the class of flows studied, but predicts incorrectly unbounded increase of the ratio $h'_{t_{rms}}/h'_{rms}$ in the wake region, with increasing $Re_{\tau^\star}$. This deficiency can be corrected only using a weak Reynolds analogy, i.e. the exact truncated-to-2oMs relation. For all of the flows considered in the present database, appropriate constant values of $c_{h'_t u'}$, $c_{u'v'}/c_{h'_t v'}$ provide a simple correlation that fits well the DNS data, but remains specific to the class of VCW flows.

The study of transport equations for the enthalpy variance $\overline{\rho h''^2}$ and fluxes $\overline{\rho h'' u_i''}$ is probably the only way to analyse the observed strong and complex dependence of Pr_T on both $Re_{\tau^\star}$ and $\bar{M}_{CL_x}$ in the near-wall region ($y^\star \lessapprox 15$). With the exception of turbulent diffusion which, in $(\cdot)^\star$ units, is practically $\bar{M}_{CL_x}$-independent, all of the other terms in the budgets of the transport equation for $\overline{\rho h''^2}$ show strong $\bar{M}_{CL_x}$-dependence in the near-wall region. It is believed that further study of the budgets of these transport equations will provide insight into the complexity of the very-near-wall flow.

Detailed data of the various moments, correlations and p.d.f.s studied in the paper, for flows with different non-dimensional enthalpy rise $(\bar{h}_{CL} - \bar{h}_w)/(\frac{1}{2}\bar{u}_{CL}^2)$, are necessary to parametrise the findings of this work for general compressible wall turbulence. Another important perspective is obtaining DNS data of compressible wall turbulence at higher Re, this being a global need, as currently available Reynolds numbers in the literature lag by almost one decade incompressible flow DNS.

Funding. The computations reported in the present work were performed using HPC resources allocated at PRACE–JUWELS (project 2021-240083) GENCI–IDRIS/TGCC/CINES (grants 2010–022139 to 2022–022139) and at ICS–UPMC (ANR–10–EQPX–29–01).

Declaration of interests. The authors report no conflict of interest.

Data availability statement. Data will be made available at http://www.aerodynamics.fr/DNS_database.

Author ORCIDs.
G.A. Gerolymos https://orcid.org/0000-0003-3207-5659;
I. Vallet https://orcid.org/0000-0003-1286-831X.

Author contributions. The authors are listed alphabetically and have both contributed equally in the entire work reported in the paper, and in writing the paper.

References

Bagheri, N., Strataridakis, C. & White, B.R. 1992 Measurements of turbulent boundary-layer Prandtl numbers and space–time temperature correlations. *AIAA J.* **30** (1), 35–42.

Bernardini, M. & Pirozzoli, S. 2011 Turbulence in supersonic boundary-layers at moderate Reynolds numbers. *J. Fluid Mech.* **688**, 120–168.

Coleman, G.N., Kim, J. & Moser, R.D. 1995 A numerical study of turbulent supersonic isothermal-wall channel flow. *J. Fluid Mech.* **305**, 159–183.

DEBIÈVE, J.F., DUPONT, P., SMITH, D.R. & SMITH, A.J. 1997 Supersonic turbulent boundary-layer subjected to step changes in wall temperature. *AIAA J.* **35** (1), 51–57.

VAN DRIEST, E.R. 1951 Turbulent boundary-layer in compressible fluids. *J. Aerosp. Sci.* **18** (3), 145–160.

DUAN, L., BEEKMAN, I. & MARTÍN, M.P. 2011 Direct numerical simulation of hypersonic turbulent boundary-layers – Part 3. Effect of Mach-number. *J. Fluid Mech.* **672**, 245–267.

FOYSI, H., SARKAR, S. & FRIEDRICH, R. 2004 Compressibility effects and turbulence scalings in supersonic channel flow. *J. Fluid Mech.* **509**, 207–216.

GAVIGLIO, J. 1987 Reynolds analogies and experimental study of heat transfer in the supersonic boundary-layer. *Intl J. Heat Mass Transfer* **30**, 911–926.

GEROLYMOS, G.A. 1990 Implicit multiple-grid solution of the compressible Navier–Stokes equations using k-ε turbulence closure. *AIAA J.* **28** (10), 1707–1717.

GEROLYMOS, G.A., SÉNÉCHAL, D. & VALLET, I. 2009 Very-high-order WENO schemes. *J. Comput. Phys.* **228**, 8481–8524.

GEROLYMOS, G.A., SÉNÉCHAL, D. & VALLET, I. 2010 Performance of very-high-order upwind schemes for DNS of compressible wall-turbulence. *Intl J. Numer. Meth. Fluids* **63**, 769–810.

GEROLYMOS, G.A., SÉNÉCHAL, D. & VALLET, I. 2013 Wall effects on pressure fluctuations in turbulent channel flow. *J. Fluid Mech.* **720**, 15–65.

GEROLYMOS, G.A. & VALLET, I. 2014 Pressure, density, temperature and entropy fluctuations in compressible turbulent plane channel flow. *J. Fluid Mech.* **757**, 701–746.

GEROLYMOS, G.A. & VALLET, I. 2016 The dissipation tensor ε_{ij} in wall turbulence. *J. Fluid Mech.* **807**, 386–418.

GEROLYMOS, G.A. & VALLET, I. 2018 Correlation coefficients of thermodynamic fluctuations in compressible aerodynamic turbulence. *J. Fluid Mech.* **851**, 447–478.

GEROLYMOS, G.A. & VALLET, I. 2023 Scalings of pressure fluctuations in compressible turbulent plane channel flow. *J. Fluid Mech.* **958**, A19.

GUARINI, S.E., MOSER, R.D., SHARIFF, K. & WRAY, A. 2000 Direct numerical simulation of a supersonic turbulent boundary-layer at Mach 2.5. *J. Fluid Mech.* **414**, 1–33.

HADJADJ, A., BEN NASR, O., SHADLOO, M.S. & CHAUDHURI, A. 2015 Effect of wall temperature in supersonic turbulent boundary-layers: a numerical study. *Intl J. Heat Mass Transfer* **81**, 426–438.

HOYAS, S., OBERLACK, M., ALCÁNTARA-ÁVILA, F., KRAHEBERGER, S. & LAUX, J. 2022 Wall turbulence at high friction Reynolds numbers. *Phys. Rev. Fluids* **7**, 014602.

HUANG, J., DUAN, L. & CHOUDHARI, M.M. 2022 Direct numerical simulation of hypersonic turbulent boundary layers: effect of spatial evolution and Reynolds number. *J. Fluid Mech.* **804**, A3.

HUANG, P.G., COLEMAN, G.N. & BRADSHAW, P. 1995 Compressible turbulent channel flows: DNS results and modelling. *J. Fluid Mech.* **305**, 185–218.

KISTLER, A.L. 1959 Fluctuation measurements in a supersonic turbulent boundary-layer. *Phys. Fluids* **2**, 290–297.

KROGSTAD, P.Å. & TORBERGSEN, L.E. 2000 Invariant analysis of turbulent pipe flow. *Flow Turbul. Combust.* **64**, 161–181.

LE RIBAULT, C. & FRIEDRICH, R. 1997 Investigation of transport equations for turbulent heat fluxes in compressible flows. *Intl J. Heat Mass Transfer* **40** (11), 2721–2738.

LEE, M. & MOSER, R.D. 2015 DNS of turbulent channel flow up to $Re_\tau \approx 5200$. *J. Fluid Mech.* **774**, 395–415.

LUSHER, D.J. & COLEMAN, G.N. 2022 Numerical study of compressible wall-bouned turbulence – the effect of thermal wall conditions on the turbulent Prandtl number in the low-supersonic régime. *Intl J. Comput. Fluid Dyn.* **36** (9), 797–815.

MEIER, H.U. & ROTTA, J.C. 1971 Temperature distributions in supersonic turbulent boundary-layers. *AIAA J.* **9** (11), 2149–2156.

MODESTI, D. & PIROZZOLI, S. 2016 Reynolds and Mach number effects in compressible turbulent channel. *Intl J. Heat Fluid Flow* **59**, 33–49.

MODESTI, D., SATHYANARAYANA, S., SALVADORE, F. & BERNARDINI, M. 2022 Direct numerical simulation of supersonic turbulent flows over rough surfaces. *J. Fluid Mech.* **942**, A44.

MORINISHI, Y., TAMANO, S. & NAKABAYASHI, K. 2004 Direct numerical simulation of compressible turbulent channel flow between adiabatic and isothermal walls. *J. Fluid Mech.* **502**, 273–308.

MORKOVIN, M.V. 1962 Effects of compressibility on turbulent flows. In *Mechanics of Turbulence (Proceedings of the International Colloquium, August 28–September 2, 1961, Marseille, [fra])* (ed. A. Favre), Colloques Internationaux du CNRS, vol. 108, pp. 367–380. Editions du CNRS.

PIROZZOLI, S. & BERNARDINI, M. 2013 Probing high-Reynolds-number effects in numerical boundary-layers. *Phys. Fluids* **25**, 021704.

ROTTA, J.C. 1964 Temperatureverteilungen in der turbulenten grenzschicht an der ebenen platte. *Intl J. Heat Mass Transfer* **7**, 215–228.

SHAHAB, M.F., LEHNASCH, G., GATSKI, T.B. & COMTE, P. 2011 Statistical characteristics of an isothermal, supersonic developing boundary layer flow from DNS data. *Flow Turbul. Combust.* **86**, 369–397.

SMITS, A.J. & DUSSAUGE, J.P. 2006 *Turbulent Shear Layers in Supersonic Flow*. Springer.

SONG, Y., ZHANG, P., LIU, Y. & XIA, Z. 2022 Central mean temperature scaling in compressible turbulent channel flows with symmetric isothermal boundaries. *Phys. Rev. Fluids* **7**, 044606 (erratum **7** 089901(E)).

STOER, J. & BULIRSCH, R. 1993 *Introduction to Numerical Analysis*. Springer.

SUMAN, S. & GIRIMAJI, S.S. 2013 Velocity-gradient dynamics in compressible turbulence: characterization of pressure-Hessian tensor. *Phys. Fluids* **25**, 125103.

TRETTEL, A. & LARSSON, J. 2016 Mean velocity scaling for compressible wall turbulence with heat transfer. *Phys. Fluids* **28**, 026102.

WARDANA, I.N.G., UEDA, T. & MIZOMOTO, M. 1995 Velocity-temperature correlation in strongly heated channel flow. *Exp. Fluids* **18**, 454–461.

YAO, J. & HUSSAIN, F. 2020 Turbulence statistics and coherent structures in compressible turbulent channel flow. *Phys. Rev. Fluids* **5**, 084603.

YU, M., XU, C.X. & PIROZZOLI, S. 2020 Compressibility effects on pressure fluctuations in compressible turbulent channel flows. *Phys. Rev. Fluids* **5**, 113401.

ZHANG, C., DUAN, L. & CHOUDHARI, M.M. 2017 Effect of wall cooling on boundary-layer-induced pressure fluctuations at Mach 6. *J. Fluid Mech.* **822**, 5–30.

ZHANG, C., DUAN, L. & CHOUDHARI, M.M. 2018 Direct numerical simulation database for supersonic and hypersonic turbulent boundary-layers. *AIAA J.* **56**, 4297–4311.

ZHANG, Y.S., BI, W.T., HUSSAIN, F. & SHE, Z.S. 2014 A generalized Reynolds analogy for compressible wall-bounded turbulent flows. *J. Fluid Mech.* **739**, 392–420.